

# Secondary instability of a temporally growing mixing layer

By RALPH W. METCALFE,

Department of Mechanical Engineering, University of Houston, Houston, TX 77004, USA

STEVEN A. ORSZAG,

Applied & Computational Mathematics, Princeton University, Princeton, NJ 08544, USA

MARC E. BRACHET,

CNRS, Observatoire de Nice, 06-Nice, France

SURESH MENON

Flow Research Company, 21414-68th Avenue South, Kent, WA 98032, USA

AND JAMES J. RILEY

Department of Mechanical Engineering, University of Washington, Seattle, WA 98195, USA

(Received 31 October 1985 and in revised form 28 March 1987)

The three-dimensional stability of two-dimensional vortical states of planar mixing layers is studied by direct numerical integration of the Navier–Stokes equations. Small-scale instabilities are shown to exist for spanwise scales at which classical linear modes are stable. These modes grow on convective timescales, extract their energy from the mean flow and exist at moderately low Reynolds numbers. Their growth rates are comparable with the most rapidly growing inviscid instability and with the growth rates of two-dimensional subharmonic (pairing) modes. At high amplitudes, they can evolve into pairs of counter-rotating, streamwise vortices, connecting the primary spanwise vortices, which are very similar to the structures observed in laboratory experiments. The three-dimensional modes do not appear to saturate in quasi-steady states as do the purely two-dimensional fundamental and subharmonic modes in the absence of pairing. The subsequent evolution of the flow depends on the relative amplitudes of the pairing modes. Persistent pairings can inhibit three-dimensional instability and, hence, keep the flow predominantly two-dimensional. Conversely, suppression of the pairing process can drive the three-dimensional modes to more chaotic, turbulent-like states. An analysis of high-resolution simulations of fully turbulent mixing layers confirms the existence of rib-like structures and that their coherence depends strongly on the presence of the two-dimensional pairing modes.

---

## 1. Introduction

Free shear flows, like those of mixing layers and jets, differ from wall-bounded flows in that they typically have inflexional mean velocity profiles and, hence, are subject to inviscid instabilities. Thus, it may be thought that the process of transition to turbulence in free shear flows would be directly amenable to analysis. Indeed, observations by Winant & Browand (1974), Brown & Roshko (1974), Wygnanski *et al.* (1979), Ho & Huang (1982), Hussain (1983*a*) and others show the central role played by two-dimensional dynamic processes, at least through transitional regimes,

in these flows. While three-dimensional small scales are observed (Miksad 1972; Bernal *et al.* 1979), they may not necessarily destroy the large-scale two-dimensional structures (Browand & Troutt 1980, 1985). In contrast, studies of wall-bounded flows have emphasized the central role of three-dimensional effects in the breakdown to turbulence.

In this paper, we investigate the interaction between linear and nonlinear two- and three-dimensional flow states that can arise during the early stages of evolution of a temporally growing turbulent mixing layer. It is shown that certain two-dimensional, nonlinear states (coherent, spanwise vortical modes) are strongly unstable to small, three-dimensional perturbations, and that these perturbations can evolve into streamwise, counter-rotating vortices similar to those observed experimentally (Bernal 1981; Bernal & Roshko 1986) and modelled analytically (Pierrehumbert & Widnall 1982; Lin & Corcos 1984). We find that the two- or three-dimensional character of the early stages of the mixing layer depends crucially on the initial conditions, as there is close competition between the various modes of instability.

The approach followed here is similar to that used by Orszag & Patera (1980, 1983) in their study of secondary instabilities in wall-bounded flows. The parallel laminar flow is perturbed initially by either a linear or a finite-amplitude two-dimensional disturbance that is allowed to evolve and to saturate in a quasi-steady state. The stability of this finite-amplitude vortical state to both subharmonic (pairing) two-dimensional modes and smaller-scale three-dimensional modes is then studied by numerical solution of the full three-dimensional time-dependent Navier–Stokes equations. To relate these simulations to the evolution of a turbulent mixing layer, we also examine the interaction between the evolving two-dimensional modes in their linear and nonlinear states and a broadband, three-dimensional background noise spectrum.

The character of the pairing instability was first explained theoretically by Kelly (1967), and numerically by Patnaik, Sherman & Corcos (1976) and Collins (1982) for stratified flows, and by Riley & Metcalfe (1980) and Pierrehumbert & Widnall (1982) for unstratified flows. The nature of the two-dimensional vortical pairing as well as a model for streamwise vortical motion have been investigated numerically and theoretically (Corcos & Sherman 1984; Corcos & Lin 1984; Lin & Corcos 1984). Experimentally, coherent pairing of large-scale vortical structures in turbulent mixing layers at high Reynolds numbers was identified by Brown & Roshko (1974). Significant secondary three-dimensional instabilities in these flows have been observed by Breidenthal (1981), Bernal (1981) and Bernal & Roshko (1986). The importance of these instabilities and their sensitivity to upstream perturbations has been demonstrated experimentally by Hussain & Zaman (1978), Oster & Wygnanski (1982) and Ho & Huang (1982) among others. There is an excellent and comprehensive review of the very extensive literature on this topic by Ho & Huerre (1984).

Pierrehumbert & Widnall (1982) examined the linear two- and three-dimensional instabilities of a spatially periodic inviscid shear layer in a study closely related to the present one. They considered the stability characteristics of the model family of two-dimensional vortex-modified mixing layers with velocity fields

$$\left. \begin{aligned} u &= \frac{\sinh z}{\cosh z - \rho \cos x}, \\ w &= -\frac{\rho \sin x}{\cosh z - \rho \cos x} \end{aligned} \right\} \quad (1.1)$$

(Stuart 1967) for  $0 \leq \rho < 1$ ,† and studied subharmonic pairing instabilities and a ‘translative’ three-dimensional instability. In contrast, we consider here both the linear and nonlinear stability characteristics of time-developing viscous shear layers. The three-dimensional secondary instability that we study is both the analogue of the translative instability and a generalization of the instability analysed by Orszag & Patera (1983) for wall-bounded flows. In the nonlinear state, this instability is manifest as the streamwise, counter-rotating vortices (Bernal 1981; Bernal & Roshko 1986) or ‘ribs’ (Hussain 1983*a*) seen in laboratory experiments.

## 2. Numerical methods

The Navier–Stokes equations are solved in the form

$$\frac{\partial \mathbf{v}}{\partial t} = \mathbf{v} \times \boldsymbol{\omega} - \nabla \pi + \nu \nabla^2 \mathbf{v}, \quad (2.1)$$

$$\nabla \cdot \mathbf{v} = 0, \quad (2.2)$$

where  $\boldsymbol{\omega} = \nabla \times \mathbf{v}$  is the vorticity and  $\pi = p + \frac{1}{2}|\mathbf{v}|^2$  is the pressure head. Periodic boundary conditions are applied in the streamwise  $x$  and spanwise  $y$  directions, where

$$\left. \begin{aligned} \mathbf{v}\left(x + \frac{4\pi}{\alpha}, y, z, t\right) &= \mathbf{v}(x, y, z, t), \\ \mathbf{v}\left(x, y + \frac{2\pi}{\beta}, z, t\right) &= \mathbf{v}(x, y, z, t), \end{aligned} \right\} \quad (2.3)$$

while the flow is assumed quiescent ( $\mathbf{v} \rightarrow U_{\pm} \hat{x}$ ;  $U_{\pm}$  const.) as  $z \rightarrow \pm \infty$ . Note that the assumed periodicity length  $B$  is  $4\pi/\alpha$  (or  $8\pi/\alpha$ ) to accommodate both the fundamental mode, with  $x$ -wavenumber  $\alpha$ , and its subharmonic, with  $x$ -wavenumber  $\frac{1}{2}\alpha$  (or  $\frac{1}{4}\alpha$ ).

Pierrehumbert & Widnall (1982) point out that Floquet theory implies that the Navier–Stokes equations linearized about a flow periodic in  $x$  admit solutions of the more general form  $\mathbf{v}(x, y, z) = e^{i\gamma x} \mathbf{V}(x, y, z)$ , where  $\mathbf{V}$  is periodic in  $x$  with the same periodicity as the basic flow and  $\gamma$  is arbitrary. However, Pierrehumbert & Widnall consider only the subharmonic and fundamental cases. The analysis, which has not yet been done for more general  $\gamma$ , may be able to address more precisely such phenomena as the ‘collective interaction’ described in experiments by Ho & Nosseir (1981). Indeed, Busse & Clever (1979) point out the importance of these general  $\gamma$ -modes in Bénard convection. The present study is restricted to  $\gamma$  being a half-integer multiple of the fundamental wavenumber because our code has the periodicity condition (2.3). Numerical simulations (Corcos & Sherman 1984) with values of  $\gamma$  different from ours indicate that the longest wave allowed by the grid will eventually dominate, although the details of the ‘pairing’ process may differ.

Our simulations are of a temporally growing mixing layer. By avoiding the requirement of imposing inflow–outflow boundary conditions, which is essential in simulations of a spatially growing flow, a faster, more efficient code can be written.

† Note that for  $\rho \ll 1$ , the basic flow state (1.1) is of the form  $\tanh z \hat{x} + \rho \operatorname{Re} [e^{i\alpha x} \mathbf{V}(z)]$ . At wavenumber  $\alpha = 1$ , there are no fundamental two-dimensional instabilities that can compete with the subharmonic ( $\alpha = \frac{1}{2}$ ) and secondary instabilities. This flow state is an inviscid neutrally stable perturbation of the mixing layer  $\tanh z \hat{x}$ . In contrast, the results to be reported in §3 involve unstable fundamental perturbations to the mixing layer.

Thus, the temporally evolving mixing layer can be simulated at higher Reynolds numbers and with better resolution than the spatial flow for a given level of computer resources. As will be shown later, there are very important linear and nonlinear dynamic features that are common to the two flows, so a detailed analysis of numerical simulations of a temporally growing flow can yield important insight into the evolution in the spatial case. There are also significant differences between the flows, which should be addressed by future simulations using inflow–outflow boundary conditions (cf. Lowery, Reynolds & Mansour 1987).

We have used two independently written numerical codes for the simulations described in this paper. In the first, the dynamical equations are solved using pseudospectral methods in which the flow variables are expanded in the series

$$v(x, y, z, t) = \sum_{|m| < \frac{1}{2}M} \sum_{|n| < \frac{1}{2}N} \sum_{p=0}^P u(m, n, p, t) e^{im\alpha x} e^{in\beta y} T_p(Z), \quad (2.4)$$

where  $n$  and  $p$  are integers, while  $m$  is a half-integer when one pairing is allowed and a whole integer if all pairing modes are excluded. Here  $Z = f(z)$  is a transformed  $z$ -coordinate satisfying  $Z = \pm 1$  when  $z = \pm \infty$ . Two choices of  $f(z)$  have been studied:

$$Z = \tanh \frac{z}{L} \quad (|z| < \infty, \quad |Z| < 1) \quad (2.5)$$

and 
$$Z = \frac{z}{(z^2 + L^2)^{\frac{1}{2}}} \quad (|z| < \infty, \quad |Z| < 1), \quad (2.6)$$

where  $L$  is a suitable scale factor. A variant of the first transform method has been successfully applied to mixing-layer simulations by Cain, Ferziger & Reynolds (1984). With these mappings, derivatives with respect to  $z$  are evaluated pseudo-spectrally using the relations

$$\frac{\partial v}{\partial z} = \frac{1}{L} (1 - Z^2) \frac{\partial v}{\partial Z}, \quad (2.7)$$

$$\frac{\partial v}{\partial z} = \frac{1}{L} (1 - Z^2)^{\frac{1}{2}} \frac{\partial v}{\partial Z} \quad (2.8)$$

for (2.5) and (2.6), respectively.

Time-stepping is done by a fractional-step method in which the nonlinear terms are marched in time using a second-order Adams–Bashforth scheme while pressure head and viscous effects are imposed implicitly using Crank–Nicolson differencing. This scheme is globally second-order-accurate in time, despite time splitting (Orszag, Israeli & Deville 1986), because the various split operators commute in the case of quiescent boundary conditions at  $z = \pm \infty$ .

There is one further technical detail regarding this numerical method that should be discussed here. Various Poisson equations, like

$$\frac{d^2 \Pi}{dz^2} - (m^2 + n^2) \Pi = g(z) \quad (|z| < \infty), \quad (2.9)$$

are solved by expansion in the eigenfunctions of  $d^2/dz^2$ :

$$\frac{d^2}{dz^2} e_k(z) = \lambda_k e_k(z) \quad (|z| < \infty). \quad (2.10)$$

		x-wavenumber $\alpha$								
		0.25			0.5			0.75		
		Number of Chebyshev polynomials ( $P+1$ )								
$L$	17	33	65	17	33	65	17	33	65	
Hyperbolic map (2.5)										
0.5	1.534	1.375	1.238	0.579	0.501	0.457	0.160	0.150	0.150	
1	0.959	0.820	0.746	0.383	0.360	0.351	0.141	0.138	0.137	
2	0.635	0.614	0.605	0.344	0.342	0.342	0.137	0.137	0.137	
4	0.612	0.598	0.597	0.324	0.342	0.342	0.041	0.136	0.137	
8	0.539	0.597	0.597	0.115	0.322	0.342	S	0.045	0.136	
16	0.202	0.526	0.596	S	S	0.321	S	S	0.046	
Algebraic map (2.6)										
0.5	0.699	0.588	0.599	0.345	0.346	0.342	0.131	0.138	0.137	
1	0.591	0.599	0.597	0.344	0.342	0.342	0.137	0.137	0.137	
2	0.600	0.597	0.597	0.342	0.342	0.342	0.136	0.137	0.137	
4	0.597	0.597	0.597	0.325	0.342	0.342	0.371	0.136	0.137	
8	0.542	0.597	0.597	0.009	0.322	0.342	S	0.043	0.136	

TABLE 1. Growth rates  $(\text{Im}(c))$  of the Orr–Sommerfeld eigenfunctions for the mixing layer  $U_0(z) = U_0 \tanh(z/\delta_t)$ . Here the Reynolds number is  $U_0 \delta_t/\nu = 100$  and the eigenvalue is the complex wave speed  $c$  for a temporal mode of the form  $\psi(z) e^{i\alpha(x-ct)}$ . For the most rapidly growing mode listed here,  $\text{Re}(c) = 0$ . S indicates that all modes are stable with the indicated parameter values.

Thus, if

$$g(z) = \sum_{k=0}^P g_k e_k(z),$$

then

$$\Pi(z) = \sum_{k=0}^P \frac{g_k}{\lambda_k - (m^2 + n^2)} e_k(z). \tag{2.11}$$

We remark that this technique gives spectrally accurate solutions, despite the fact that the continuous version of the eigenvalue problem (2.10) has only a continuous, and hence singular, spectrum. Also, note that all the eigenvalues  $\lambda_k$  are real and non-positive; for both mappings (2.5) and (2.6), there are precisely three zero eigenvalues  $\lambda_1, \lambda_2, \lambda_3$ . One of these zero eigenmodes is physical, viz.  $e_1(z) = 1$ , but the other two are highly oscillatory and unphysical. Indeed, since the spectral (Chebyshev) derivative of  $T_p(Z)$  vanishes except at  $Z = \pm 1$ ,  $e_2(Z) = T_p(Z)$  is a zero eigenfunction of  $d^2/dz^2$ ;  $T_p(Z_j) = (-1)^j$  at the Chebyshev collocation points  $Z_j = \cos \pi j/P$ . The third zero eigenmode oscillates and grows roughly like  $z$ . When  $m = n = 0$ , the incompressibility constraint (2.2) requires that this mode of the  $z$ -velocity field vanish identically so there is no difficulty with zero-pressure eigenvalues  $\lambda_1, \lambda_2, \lambda_3$ .

Comparisons of the behaviour of linear Orr–Sommerfeld eigenmodes obtained using mappings (2.5) and (2.6) show that (2.6) gives a superior representation of these modes unless  $L$  is fine tuned, which is not convenient in the nonlinear dynamic runs. Some representative results are given in table 1. Notice that as  $\alpha$  increases, the optimal choice of map scale  $L$  decreases. Also, notice that the accuracy of the eigenvalue is much more sensitive to  $L$  for the hyperbolic tangent mapping (2.5) than for (2.6).

There is one case in which it seems that the hyperbolic tangent mapping (2.5) is

more convenient than the algebraic mapping (2.6). This flow is the generalized Taylor–Green vortex flow that develops from the initial conditions

$$\left. \begin{aligned} u(x, y, z, 0) &= \sin x \cos y / \cosh^2 z, \\ v(x, y, z, 0) &= -\cos x \sin y / \cosh^2 z, \\ w(x, y, z, 0) &= 0. \end{aligned} \right\} \quad (2.12)$$

The evolution of this flow seems best studied, either by power series or initial value methods, using (2.5) with  $L = 1$ . The time evolution of this free shear flow is remarkably similar to that of the periodic Taylor–Green vortex (Brachet *et al.* 1983).

This nonlinear, time-dependent Navier–Stokes code has been tested for the generalized Taylor–Green vortex flow (2.12) and also for linearized eigenfunction behaviour, with satisfactory agreement being achieved with power series in  $t$  (Brachet *et al.* 1983) and linear behaviour, respectively.

The second code used in the simulations is similar to the one just described, except that sine and cosine expansions in  $z$  were used instead of Chebyshev polynomials (2.4). Thus, the transverse domain extent is finite, and care must be taken to identify possible interference effects. Comparisons with results from the first simulations as well as simulations performed on varying size domains has verified that such effects are small for the cases presented here. Aside from details of the input/output buffering routines and the size of the arrays used in the computations, the basic code structure is similar to that described in Orszag & Pao (1974).

### 3. Two-dimensional instabilities

In this and the following sections, results are reported for the evolution of initial velocity fields of the form

$$\begin{aligned} \mathbf{v}(x, y, z, 0) = U_0(z) \hat{x} + A_{10} v_{10}(z) \cos[\alpha(x + \theta)] + A_{\frac{1}{2}, 0} v_{\frac{1}{2}, 0}(z) \cos(\tfrac{1}{2}\alpha x) \\ + A_{11} v_{11}(z) \cos[\alpha(x + \phi)] \sin \beta y, \end{aligned} \quad (3.1)$$

where  $\theta$  is the phase shift between the fundamental and subharmonic modes, and  $\phi$  is the corresponding phase shift of the spanwise mode. The laminar mean profile is assumed to be  $U_0(z) = U_0 \tanh z/\delta_i$ , an approximation to the mixing-layer profile, and  $v_{ij}(z)$  is normalized so that  $\max_z |v_{ij}(z)| = 1$ . Here,  $\delta_i$  is the initial mean vorticity thickness.

The initial functions  $v_{ij}(z)$  are normally chosen as the most unstable eigenfunctions of the linear Orr–Sommerfeld equation for the appropriate wave-numbers given in (3.1) (Michalke 1964). It should be noted that the Reynolds numbers of the flows discussed below, while modest, are much greater than that of the onset of linear instability ( $R_{\text{crit}} \approx 0$ ), so that even the linear modes are effectively inviscid. In this case, damped modes may lie only in the continuous spectrum (Drazin & Reid 1981) and so are singular. Whenever (3.1) calls for such a singular contribution to the initial condition (3.1), we choose instead the flow component  $w_{nm} \equiv w_{10}$  of the fundamental mode (with  $u_{nm}$  and  $v_{nm}$  determined by incompressibility). In this representation,  $A_{10}$  is the amplitude of the fundamental two-dimensional component,  $A_{\frac{1}{2}, 0}$  is the amplitude of its subharmonic or pairing mode, and  $A_{11}$  is the amplitude of the primary three-dimensional wave with a spanwise wavelength equal to that of the fundamental two-dimensional mode. Time is non-dimensionalized by  $2U_0/\delta_i$  and space scales by

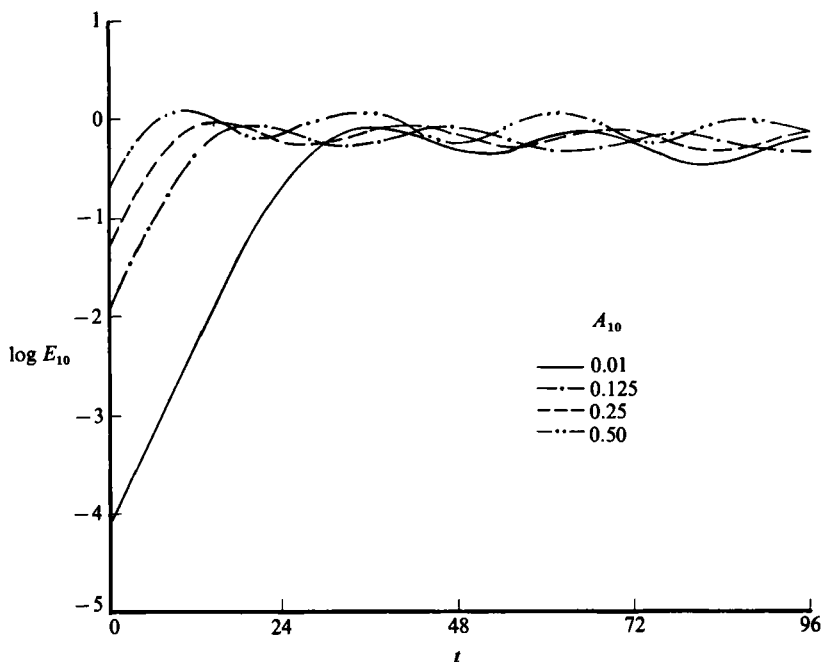


FIGURE 1. A plot of  $E_{10}(t)$  versus  $t$  for runs with  $A_{1,0} = A_{11} = 0$  and  $A_{10} = 0.5, 0.25, 0.125, 0.01$ . Here the Reynolds number is  $R = 400$ , the spectral cutoffs in (2.4) are  $M = 8, N = 1, P = 32$  (resolution  $8 \times 1 \times 32$  with no subharmonic modes), the  $x$ -wavenumber is  $\alpha = 0.4$ , and the time-step is  $\Delta t = 0.02$ . Note that the flow saturates into a vortical state nearly independent of the initial perturbation. Before such saturation occurs, the perturbation grows linearly like an Orr-Sommerfeld eigenfunction.

$\delta_i$ . The initial conditions are typically chosen so that  $A_{1,0}, A_{11} \ll A_{10}$  and  $A_{10} = 0.25$ . The Reynolds number for the undisturbed flow is  $R = U_0 \delta_i / \nu$ .

In the absence of subharmonic and three-dimensional perturbations ( $A_{1,0} = A_{11} = 0$ ), the two-dimensionally perturbed flow quickly saturates to a quasi-steady state. Figure 1 is a plot of the time evolution of the two-dimensional disturbance energy  $E_{10}(t)$  for various initial amplitudes  $A_{10}$ . The value for  $\alpha$  is taken to be 0.4446, which is the wavenumber corresponding to the largest growth rate predicted by linear theory (Michalke 1964). (The range of inviscidly unstable wavenumbers for the  $\tanh z$  profile is  $0 < \alpha < 1$ .) Here

$$E_{mn}(t) = \int_{-\infty}^{\infty} |v_{mn}(z, t)|^2 dz, \quad (3.2)$$

where

$$v_{mn}(z, t) = \sum_{p=0}^P \mathbf{u}(m, n, p, t) T_p(z) \quad (3.3)$$

and  $\mathbf{u}$  is defined by (2.4). It is apparent that  $E_{10} \dagger$  saturates into a finite-amplitude vortical state on a timescale of order 10. The independence of the peak saturation amplitude from the initial excitation amplitude except for very high initial ampli-

$\dagger$  Note that  $E_{10}$  does not precisely correspond to the energy in the fundamental mode at later times. For example, the subharmonic mode by itself will develop an  $E_{10}$  component as it rolls up (e.g. see figure 17).

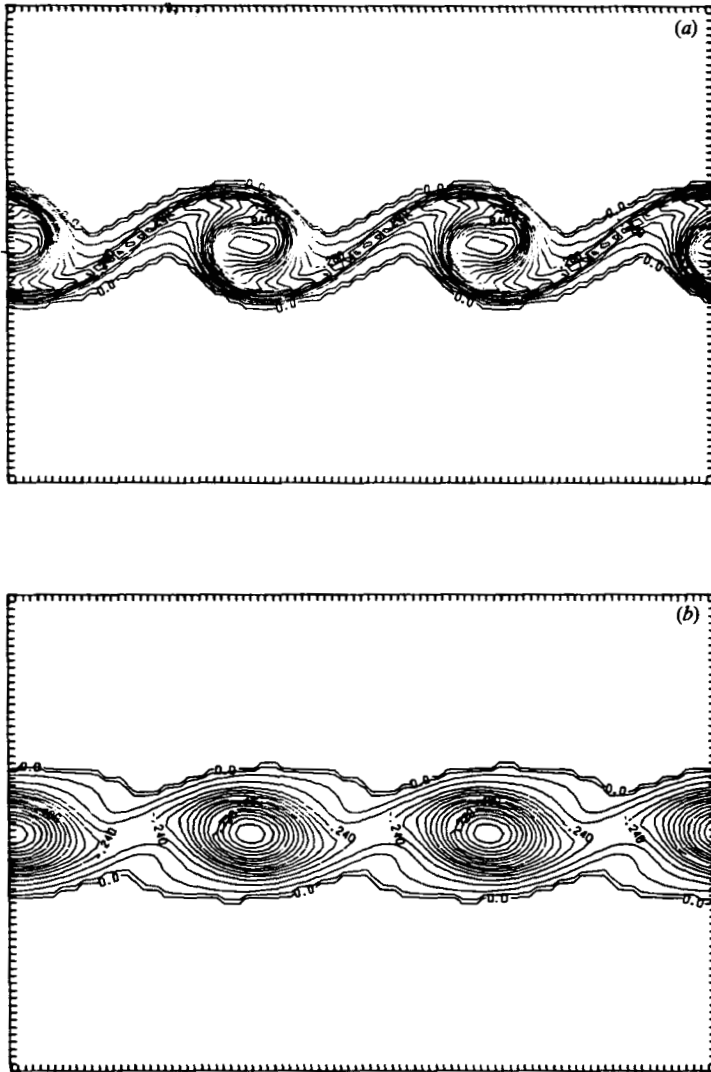


FIGURE 2. Contour plots of spanwise ( $y$ ) vorticity for the mixing layer at (a)  $t = 8$  and (b) 32 with  $R = 83$ ,  $A_{\frac{1}{2},0} = 0$ ,  $A_{10} = 0.2$ ,  $M = P = 64$  and  $N = 1$ . Contour interval is 0.07; and peak contour value is (a)  $-1.12$ , (b)  $-0.96$ .

tudes, which is evident in figure 1, has also been observed experimentally by Freymuth (1966). If we define the growth rate  $\sigma$  as

$$\sigma = \frac{dE/dt}{2E}, \quad (3.4)$$

then for linear disturbances of the form

$$\psi' = \text{Re} [q(z) e^{i\alpha(x-ct)}], \quad (3.5)$$

we have  $\sigma = \alpha c_i$ . The theoretically predicted peak growth rate of the most unstable linear mode ( $\alpha = 0.4446$ ) is  $\sigma = 0.19$ . Our growth rates, which are given later in the text, should be divided by a factor of 2 for comparison with the linear results for  $\alpha c_i$ .

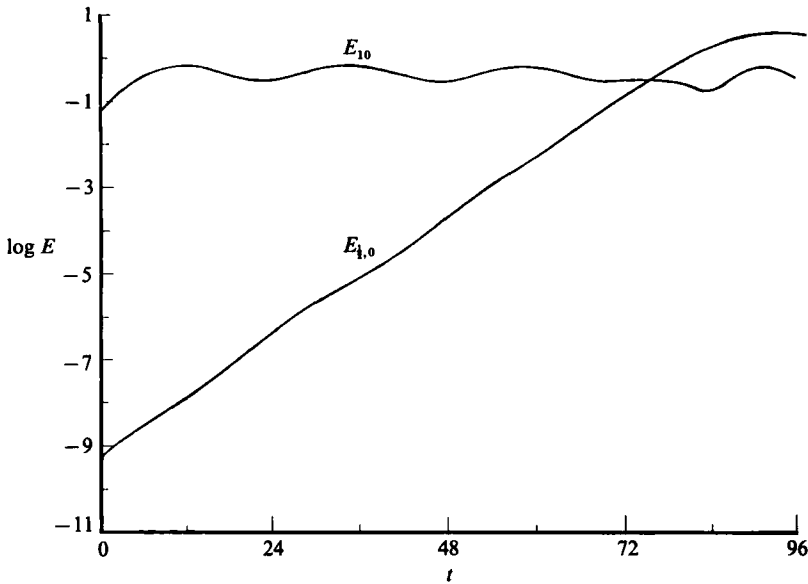


FIGURE 3. Plots of the evolution of  $E_{10}(t)$  and the two-dimensional subharmonic mode energy  $E_{1,0}(t)$ . Here  $R = 400$ ,  $A_{10} = 0.25$ ,  $A_{1,0} = 3 \times 10^{-4}$ ,  $M = 8$ ,  $N = 1$ ,  $P = 32$ ,  $\alpha = 0.5$ ,  $\Delta t = 0.02$  and  $\theta = \pi/2\alpha$  (phase difference between the two modes).

given by Michalke (1964) to reflect the different choice of  $U_0$ . In analysing these growth rates, it should be recalled that an important aspect of the saturation process is the growth in the thickness of the mixing layer as the fundamental mode rolls up. This has the effect of reducing the growth rate (based on linear theory) of a disturbance with the wavelength of the fundamental. In fact, in our simulations, saturation occurs at approximately the time at which the mixing-layer thickness has doubled, and the mode corresponding to  $E_{10}$  would no longer be linearly unstable.

Figure 2 is a plot of the instantaneous spanwise vorticity distribution in the developed two-dimensional flow for a run similar to that shown in figure 1. Note that while roll-up is occurring by  $t = 8$ , in the absence of a subharmonic mode,  $A_{1,0}$ , pairing does not take place, and the flow evolves into the nonlinear, quasi-equilibrium state shown in figure 2(b). This absence of pairing is analogous to that artificially induced by upstream forcing in experiments by Miksad (1972), Hussain & Zaman (1978), Oster & Wygnanski (1982), Ho & Huang (1982) and others. In these experiments, the forced mode is amplified without also amplifying its subharmonic. Thus, roll-up of the forced mode is achieved without pairing, creating a region in the flow characterized by large-scale, spanwise-coherent, non-pairing modes. This produces countergradient momentum fluxes, interruption in the growth of the mixing-layer thickness, and a reversal in the sign of the Reynolds stresses (Patnaik *et al.* 1976; Riley & Metcalfe 1980). That these phenomena are also observed experimentally makes this nonlinear, quasi-equilibrium state of interest in analysing the physics of the laboratory flows.

The saturated two-dimensional flow state discussed above can be unstable to subharmonic perturbations,  $A_{1,0}$  in (3.1), for suitable  $\alpha$  (Kelly 1967). In figure 3, we plot the evolution of the subharmonic perturbation energies  $E_{1,0}(t)$  as well as the fundamental two-dimensional energy  $E_{10}(t)$ . Here we choose  $A_{10} = 0.25$  and  $A_{1,0} = 3 \times 10^{-4}$ . In figure 3, the phase difference  $\theta/\alpha$  between the two modes is  $\frac{1}{2}\pi$ , so that pairing occurs. Values of  $\theta/\alpha$  other than integral multiples of  $\pi$  result in

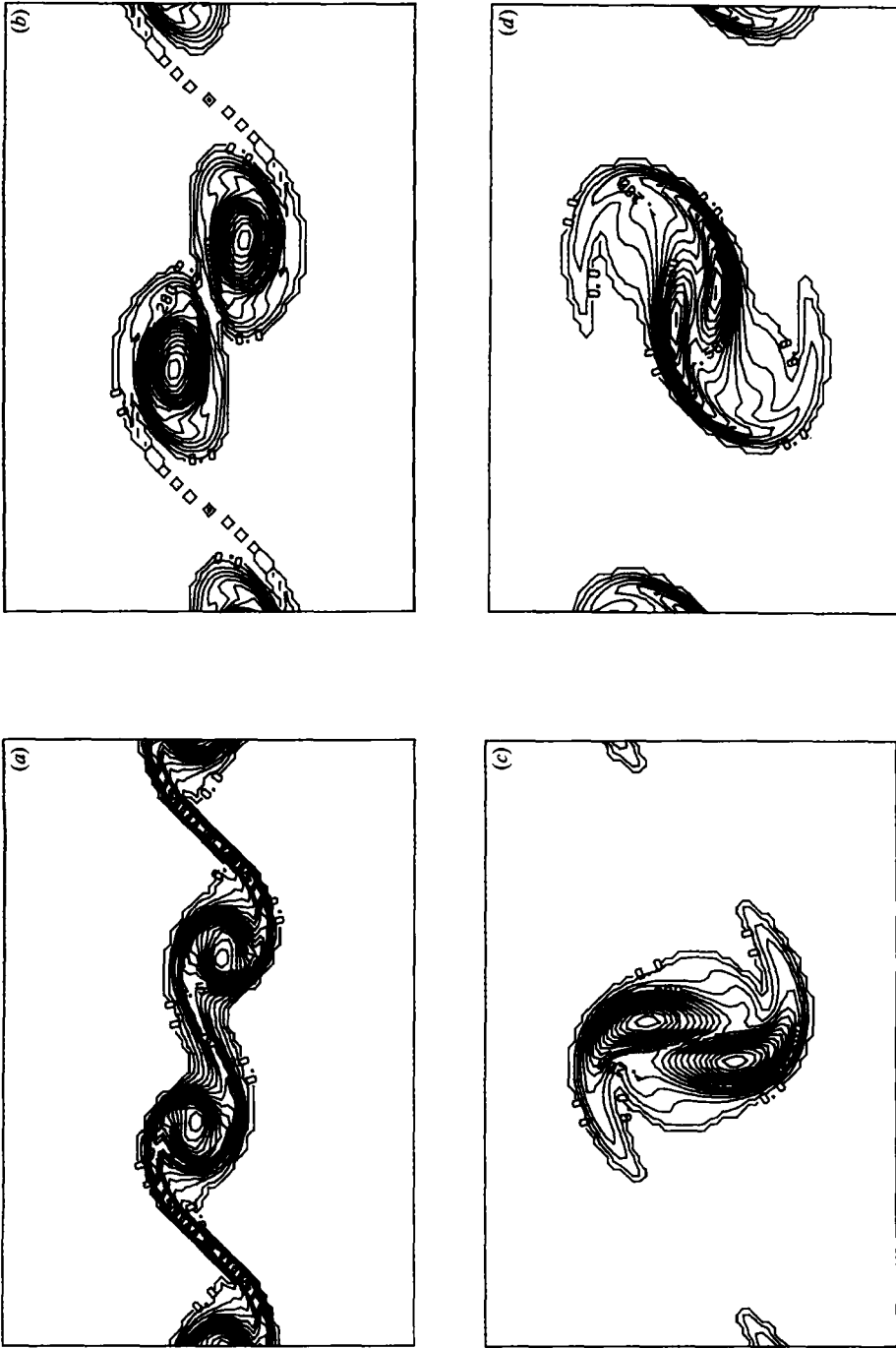


FIGURE 4. Spanwise vorticity contours at (a)  $t = 8$ , (b) 16, (c) 24, and (d) 32, during a vortex pairing run with  $R = 83$ ,  $A_{10} = 0.20$ ,  $A_{3,0} = 0.14$ ,  $M = 64$ ,  $N = 1$ ,  $P = 64$  (resolution  $64 \times 1 \times 64$ ),  $\alpha = 0.4446$ ,  $\Delta t = 0.4446$ ,  $\Delta t = 0.05$  and  $\theta = \pi/2\alpha$ . Contour interval is (a, b) 0.08, (c, d) 0.07; and peak contour value is (a) -1.28, (b) -1.20, (c) -1.12, (d) -1.05.

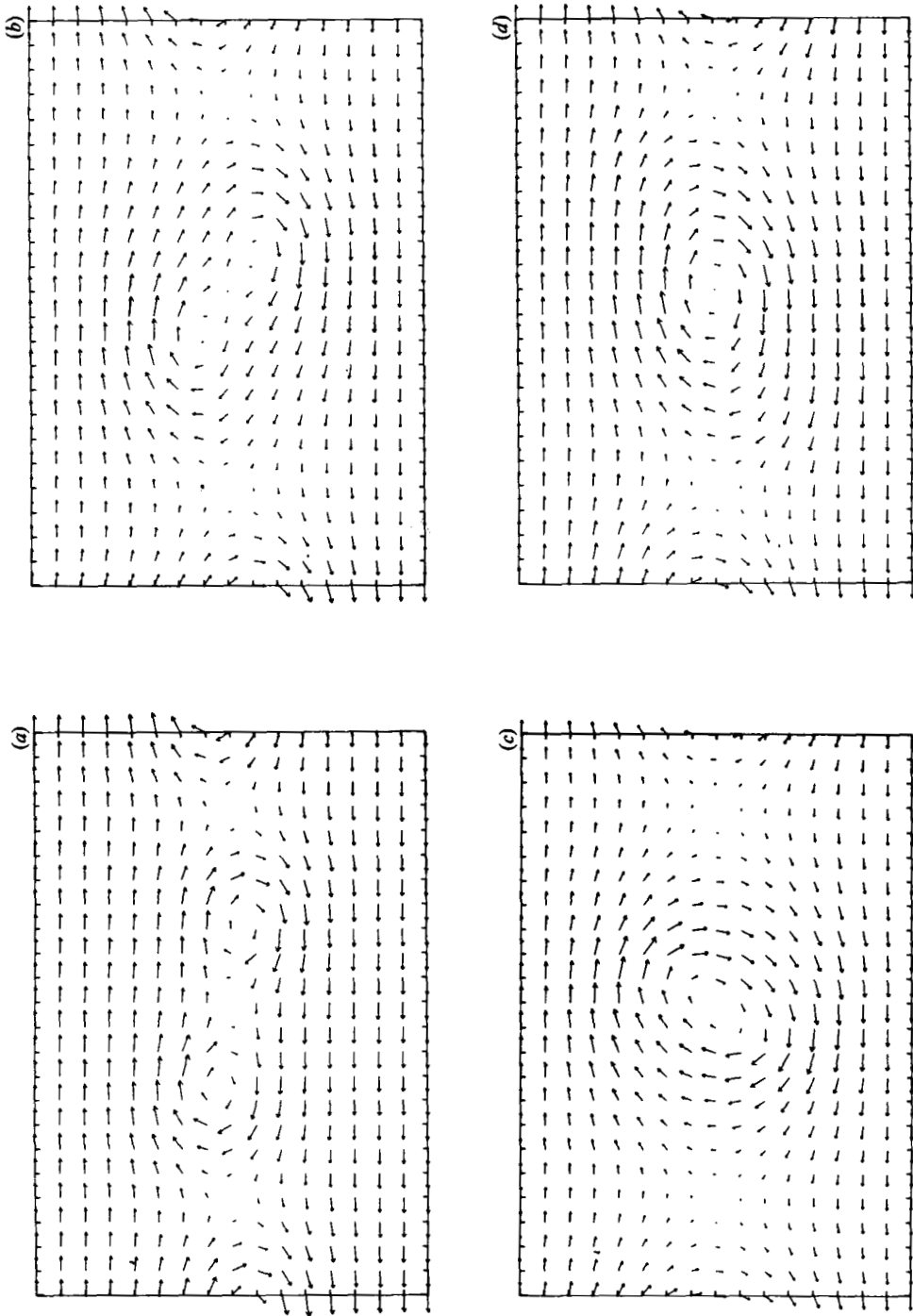


FIGURE 5. Velocity vector plots of the vortex pairing run shown in figure 4. Peak velocity is (a) 0.702, (b) 0.783, (c) 0.8, (d) 0.714.

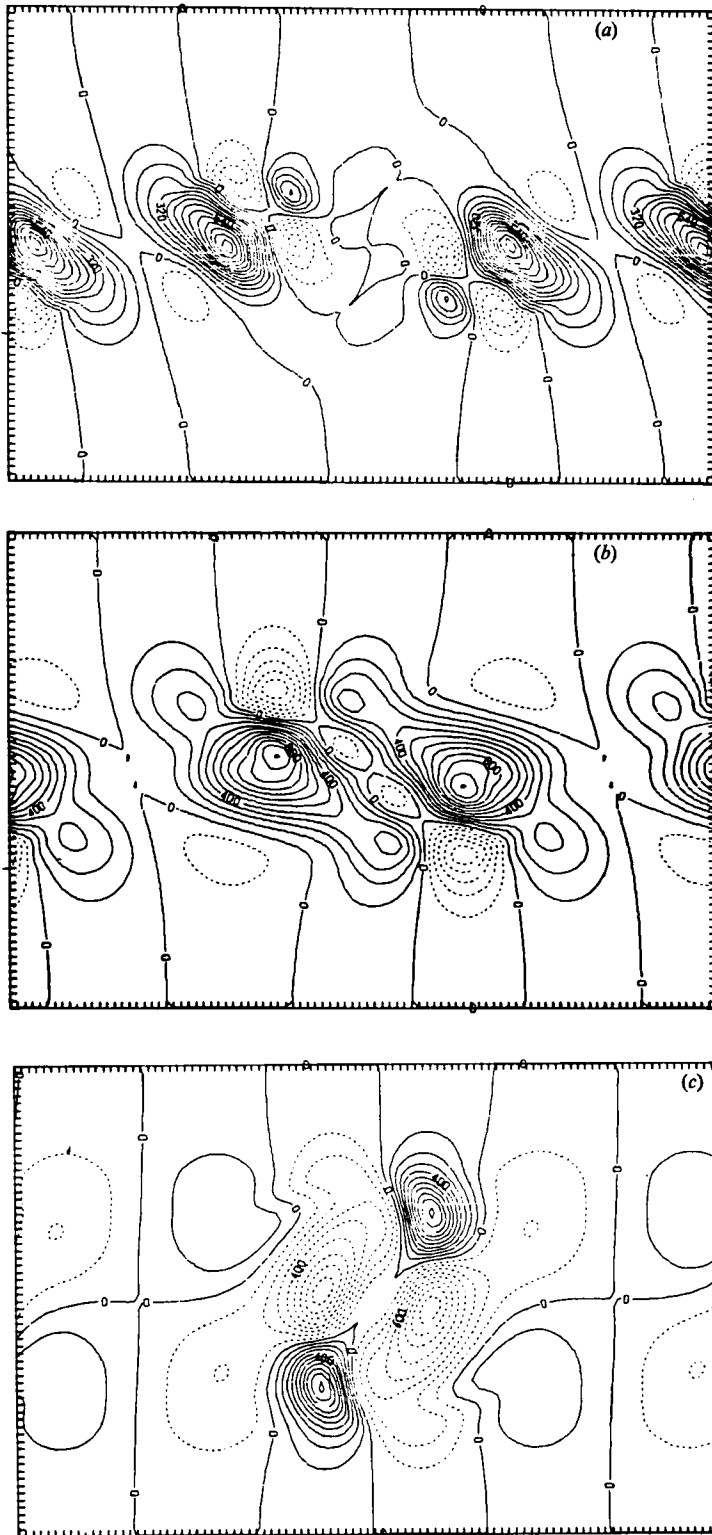


FIGURE 6(a-c). For caption see facing page.

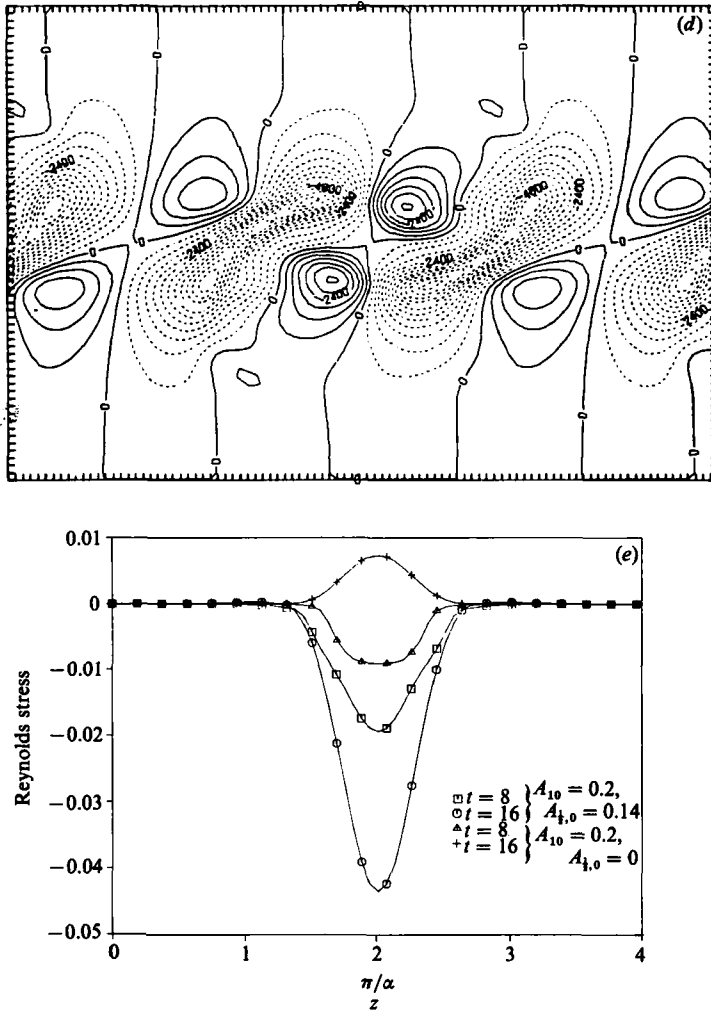


FIGURE 6. (a-d) Plots of the Reynolds stress at  $t = 8, 16, 24, 32$  respectively for the runs with both fundamental and subharmonic present (figure 4). (a) Contours are from  $-0.032$  to  $0.104$  and the contour interval is  $0.008$ ; (b)  $-0.05$  to  $0.11, 0.01$ ; (c)  $-0.08$  to  $0.1, 0.01$ ; (d)  $-0.072$  to  $0.036, 0.006$ . (e) A plot of the horizontally averaged Reynolds stress with and without pairing at different times.

pairing, while pairing is temporarily inhibited when  $\theta/\alpha$  is near  $N\pi$ , with  $N$  an integer. The cases  $\theta/\alpha = N\pi$  are anomalous, resulting in the 'shredding interaction' (Patnaik *et al.* 1976) which is rarely seen experimentally. (See Riley & Metcalfe (1980) or Ho & Huerre (1984, p. 382) for additional plots and a more detailed discussion of phase differences.) This subharmonic instability of the saturated two-dimensional vortical states is inviscid in character, as its growth rate asymptotically approaches a finite limit as  $R$  increases. The growth rate  $\sigma_{\frac{1}{2},0}$  of the amplitude of the subharmonic mode is quite significant; at  $R = 200$ ,  $\sigma_{\frac{1}{2},0} \approx 0.1$  when  $\alpha = 0.4$ , while  $\sigma_{\frac{1}{2},0} \approx 0.2$  for  $\alpha = 0.8$ . These are not significantly different from the corresponding linear inviscid growth rates of Orr-Sommerfeld modes (Michalke 1964), which are  $\sigma_{\frac{1}{2},0} \approx 0.14$  and  $0.19$ , respectively.

The evolution of the spanwise vorticity distribution during pairing instability is

shown in the contour plots in figure 4 (from Riley & Metcalfe 1980). There is strong similarity between these figures and flow visualizations of mixing layers, such as those of Winant & Browand (1974). Note that in two spatial dimensions, the lines of constant vorticity act as fluid markers much like the dye used in experiments. The evolution of the pairing process is strongly dependent on the relative initial amplitudes of the unstable modes. When  $A_{\frac{1}{2},0} \approx A_{1,0}$ , the fundamental mode rolls up first owing to its higher growth rate and shorter saturation timescale. The subharmonic continues growing after the fundamental saturates, during which time the vortex cores generated by the roll-up of the fundamental are merged into the subharmonic core. In this simulation (figure 4), the subharmonic mode  $A_{\frac{1}{2},0}$  will become saturated after about  $t = 24$ , since there is no second subharmonic mode ( $A_{\frac{1}{4},0}$ ) with which it can pair.

Some insights into the dynamics of this process can be gained from comparing figures 4 and 5. Figure 5 is a series of velocity vector plots at the same times as those in figure 4. At  $t = 8$ , the vortical motion of the fundamental cores dominates the flow and there are four nodal points: two at the centres of the vortex cores and two stagnation points at the centres of the braids. By  $t = 24$ , the vorticity peaks corresponding to the fundamental are still present (figure 4c), although they are no longer as dynamically significant as earlier (cf. figure 5a, c). At this point, there are basically two nodal points in the flow: one at the centre of the subharmonic core and the other in the region of high strain at the centre of the braid. By  $t = 32$ , the subharmonic mode has saturated and the vortex core collapsed into a quasi-equilibrium, nonlinear state like that for the unpaired fundamental (figure 2b).

As has been previously noted (e.g. Patnaik *et al.* 1976; Corcos & Sherman 1984), the importance of the pairing process to the dynamic evolution of the flow is clearly demonstrated by examining plots of the Reynolds stresses,  $-\overline{uw}$  (figure 6). From the dynamic equation for the integrated mean kinetic energy  $E_M$ ,

$$\frac{dE_M}{dt} = - \int_0^{4\pi/\alpha} \frac{\partial \overline{U}}{\partial z} \overline{uw} dz \quad (3.6)$$

(neglecting viscous effects), it can be seen that a positive Reynolds stress implies gradient momentum transport (since  $\partial U/\partial z > 0$ ) and a feed of energy from the mean flow into the perturbation field, while negative Reynolds stress produces counter-gradient momentum flux and feeds energy from the fluctuations back into the mean. During the early stages of pairing, the Reynolds stress is predominantly positive. However, by  $t = 24$  (figure 6c), large negative regions (denoted by dashed lines in the figures) have developed, and by  $t = 32$  (figure 6d), the Reynolds stress has become predominantly negative. The relevance of the pairing mode is summarized in the results for the horizontally averaged Reynolds stress as a function of  $z$  presented in figure 6(e). Without the subharmonic pairing mode, the Reynolds stress changes sign by  $t = 16$ . With the subharmonic present, however, the net Reynolds stress is still positive at  $t = 16$ . Thus, the suppression of pairing, whether caused by forcing, as in laboratory experiments (Hussain & Zaman 1978; Oster & Wignanski 1982; Ho & Huang 1982), or by eliminating the subharmonic mode, as in the numerical simulations, is associated with a reversal in the sign of the Reynolds stress.

This phenomenon is apparent in figure 3, in which the energy in the fundamental  $E_{10}$  reaches saturation by about  $t = 10$  and then begins to decay. At this point, the Reynolds stress changes sign, and a countergradient momentum flux develops. In the absence of other disturbances, this flow will then evolve into an oscillatory state

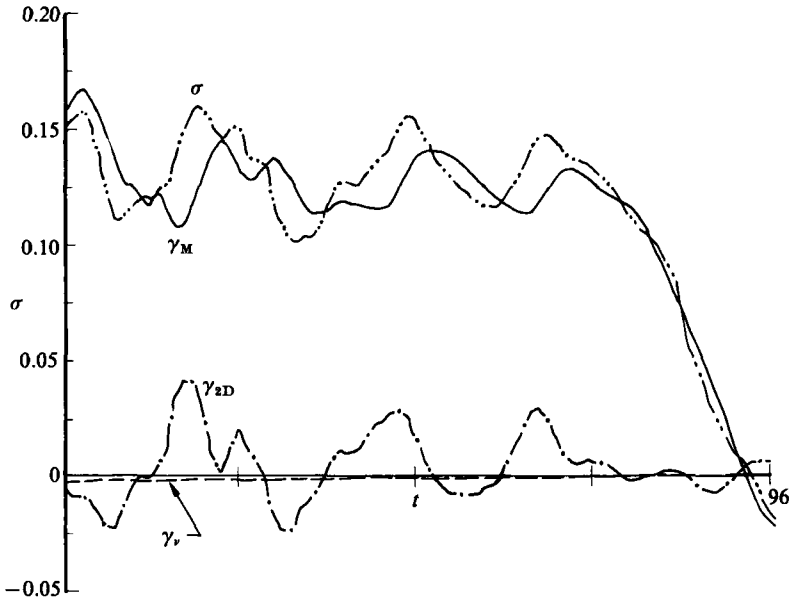


FIGURE 7. A plot of the components  $\gamma_M$ ,  $\gamma_{2D}$ ,  $\gamma_\nu$  (see (3.8)) of the growth rate  $\sigma_{\frac{1}{2},0}$  of the subharmonic mode amplitude as functions of time for a run with  $R = 200$ ,  $A_{10} = 0.25$ ,  $A_{\frac{1}{2},0} = 3 \times 10^{-5}$ ,  $M = 16$ ,  $N = 1$ ,  $P = 32$ ,  $\alpha = 0.43$  and  $\Delta t = 0.01$ .

characterized by an alternating energy exchange between the mean flow and the perturbation fields.

In terms of turbulence models, the presence of pairing is essential to maintain the positivity of transport coefficients (such as eddy viscosity). Since the eddy viscosity  $\nu_{\text{eddy}}$  is related to the Reynolds stress by

$$-\overline{uw} = \nu_{\text{eddy}} \frac{\partial \overline{U}}{\partial z}, \quad (3.7)$$

it follows that suppression of the pairing corresponds to a negative eddy viscosity. This suggests that accurate simulations of flows with inhibited pairing may require the direct calculation of large-scale structures.

The energetics of the pairing instability is revealing. Energy transfers to and from the subharmonic mode may be decomposed as

$$\frac{1}{2E_{\frac{1}{2},0}} \frac{dE_{\frac{1}{2},0}}{dt} \equiv \sigma_{\frac{1}{2},0} = \gamma_M + \gamma_{2D} + \gamma_\nu, \quad (3.8)$$

where  $\gamma_M$  involves the nonlinear interaction of the subharmonic mode with the mean flow,  $\gamma_{2D}$  the nonlinear interaction of the subharmonic mode and all other two-dimensional modes and  $\gamma_\nu$  the viscous dissipation of pairing energy. Here  $\gamma_M$  and  $\gamma_{2D}$  involve sums over nonlinear terms in the Navier–Stokes equations but are unaffected by pressure;  $\gamma_\nu$  is proportional to the enstrophy in the subharmonic mode. These transfer terms are plotted in figure 7 as a function of time. It appears that the subharmonic mode extracts most of its energy from the mean flow and that there is little net energy transfer between it and the fundamental mode. In addition, its average growth rate differs little from that in the absence of the fundamental, which is  $\sigma \approx 0.14$ . Thus, the presence of the saturated two-dimensional fundamental does

not turn off the subharmonic mode, and the growth rate of this latter mode is close to that of the fundamental two-dimensional instability. These results imply that even a small subharmonic perturbation will quickly achieve finite amplitude after the fundamental mode saturates, unless the amplitude of the fundamental is artificially amplified by forcing. In this simulation, the subharmonic mode saturates at  $t \approx 90$  at which time the growth rate becomes negative. It should be noted here that in attempting to compare these results for growth rates of the fundamental and subharmonic modes with experiments, it is necessary to account for the dispersion of the subharmonic modes (cf., for example, figure 2(b) in Ho & Huerre 1984), which is present in the spatially growing but not in the temporally growing mixing layer.

Corcos & Sherman (1984) find that the presence of the fundamental inhibits the subharmonic growth, while Pierrehumbert & Widnall (1982) find an enhancement of growth. We find that the growth rate of the subharmonic is modulated with a period related to the oscillation timescale of the nonlinear, quasi-equilibrium fundamental mode. However, the net effect on the growth of the subharmonic due to the fundamental is to decrease  $\sigma_{\frac{1}{2},0}$  slightly, from about 0.16 to 0.14. While these conclusions do agree qualitatively with those obtained by Kelly (1967) using perturbation theory, they show that the effect is quantitatively quite small.†

#### 4. Three-dimensional instabilities

The saturated two-dimensional flow is also subject to three-dimensional instabilities. While the laminar flow is inviscidly unstable only for  $\alpha^2 + \beta^2 < 1$  (Drazin & Reid 1981), the finite-amplitude two-dimensional flow can be unstable for large  $\beta$  at high Reynolds numbers. In figure 8, we plot the average three-dimensional growth rate  $\sigma_{3D}$  versus  $\beta$  of the three-dimensional disturbance energy,

$$E_{3D} = \sum_m E_{m1}(t), \quad (4.1)$$

for various Reynolds numbers when  $\alpha = 0.4$ , for a three-dimensional linear perturbation to a saturated, two-dimensional quasi-equilibrium flow. The behaviour of these spanwise perturbations to the full nonlinear, quasi-equilibrium flow state is qualitatively similar to that found in the multiple timescale analysis of Klassen & Peltier (1985). Analysis of these results suggests the conjectures that, as  $R$  increases, for a fixed  $\beta$ ,  $\sigma_{3D}$  approaches a finite limit (so the secondary instability discussed is inviscid in character) and that the instability turns off for

$$\beta > \beta_{\text{crit}} \approx \frac{1}{3}R^{\frac{1}{2}}. \quad (4.2)$$

Although the mean flow,  $\tanh z$ , is both viscously and inviscidly stable for  $\beta > 1$ , the saturated, two-dimensional disturbed flow is strongly unstable at these scales, with disturbances growing at rates near those of the inviscid two-dimensional subharmonic instability, as shown in figure 9. When the two-dimensional modes saturate, the three-dimensional modes can achieve finite amplitudes on convective timescales and thereby modify significantly the later evolution of the flow.

Like the two-dimensional modes, the three-dimensional modes evolve into vortical states at large amplitudes. One important manifestation of these instabilities is the counter-rotating vortices, or 'ribs', that develop in the braids between the two-

† Recently, Z. S. She (private communication) has developed a global theory of two-dimensional vortex coalescence.

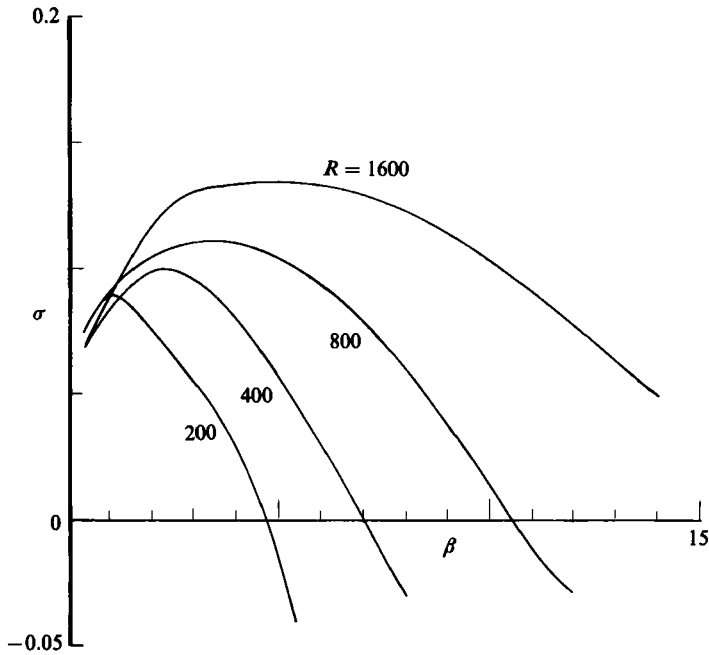


FIGURE 8. A plot of the computed three-dimensional growth rate  $\sigma_{3D}$  (see (4.3)) as a function of the spanwise wavenumber  $\beta$  for various Reynolds numbers. Here  $\alpha = 0.4$ .

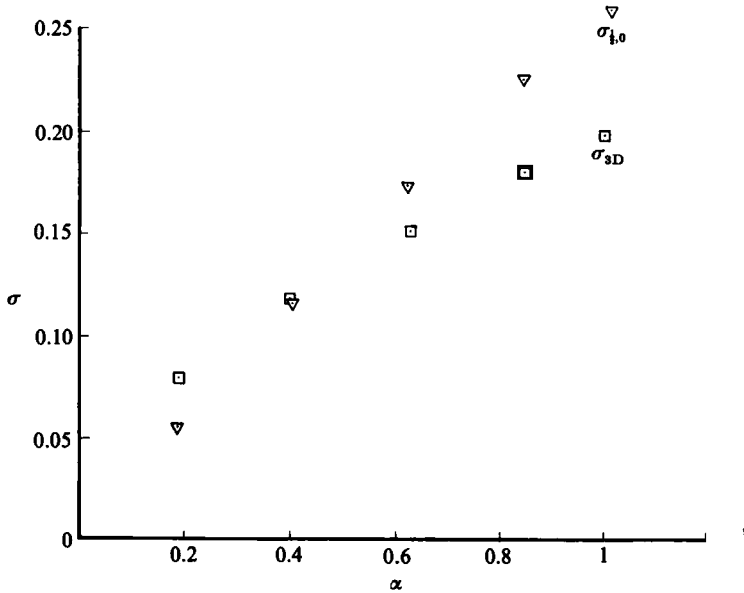


FIGURE 9. A plot of the computed subharmonic growth rate  $\sigma_{\frac{1}{2},0}$  and three-dimensional growth rate  $\sigma_{3D}$  as a function of  $\alpha$  at  $R = 400$  and  $\beta = 0.8$ . Note that the wavenumber of the pairing mode is  $\frac{1}{2}\alpha$ .

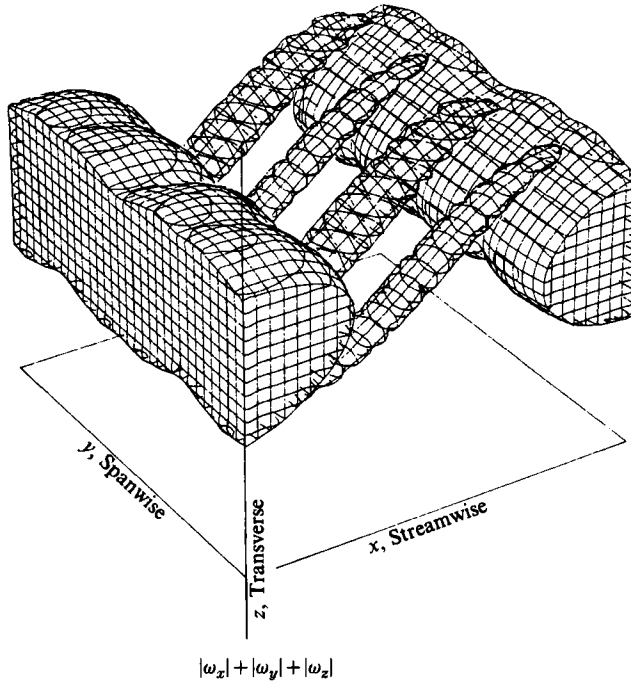


FIGURE 10. A three-dimensional perspective plot of surfaces having a value equal to 50% of the peak of the sum of the absolute values of all three vorticity components for a run with  $R = 56$  (at  $t = 12$ ),  $M = N = P = 64$ ,  $\alpha = 0.4446$ ,  $\Delta t = 0.05$ ,  $A_{10} = 0.22$ ,  $A_{\frac{1}{2},0} = 0$ ,  $A_{11} = 0.003$ ,  $\beta = 0.8892$  at  $t = 12$ .

dimensional vortex cores. In figure 10, we show a three-dimensional perspective plot of surfaces having a value of 50% of the peak of the sum of the absolute values of all three vorticity components. The data are from a simulation with  $A_{10} = 0.22$ ,  $A_{\frac{1}{2},0} = 0$ ,  $A_{11} = 0.003$ ,  $R = 28$ ,  $\alpha = 0.4446$  and  $\beta = 0.8892$  at  $t = 12$ . The saturated, two-dimensional vortex cores are shown spanning the domain, and the two pairs of counter-rotating, streamwise vortices ( $\beta = 2\alpha$ ), which have evolved from a low-amplitude, linear perturbation, have developed in the high-strain braid region. These are very similar to the structures seen experimentally by Breidenthal (1981) and Bernal (1981; Bernal & Roshko 1986) and modelled by Lin & Corcos (1984) and Nagata & Busse (1983) for a bounded shear flow; they will be discussed in more detail in §5. In this and subsequent simulations, the choice  $\phi/\alpha = \frac{1}{2}\pi$  (equation (3.1)) was made. The choice  $\phi/\alpha = N\pi$  appeared to produce anomalous behaviour in the evolution of the ribs, somewhat analogous to the two-dimensional shredding interaction when  $\phi/\alpha = N\pi$ .

The cutoff as  $\beta \rightarrow \beta_{\text{crit}}$  (4.2) is mainly due to increasing viscous damping, as nonlinear transfers are less dependent on  $\beta$ . This point is suggested by the results plotted in figure 11, which shows the contributions to the growth rate  $\sigma_{3D}$ :

$$\frac{1}{2E_{3D}} \frac{dE_{3D}}{dt} \equiv \sigma_{3D} = \gamma_M + \gamma_{2D} + \gamma_\nu \quad (4.3)$$

Here  $\gamma_M$  involves the nonlinear interaction of the three-dimensional and mean flows, and  $\gamma_{2D}$  the interaction of the three-dimensional and two-dimensional energy. The

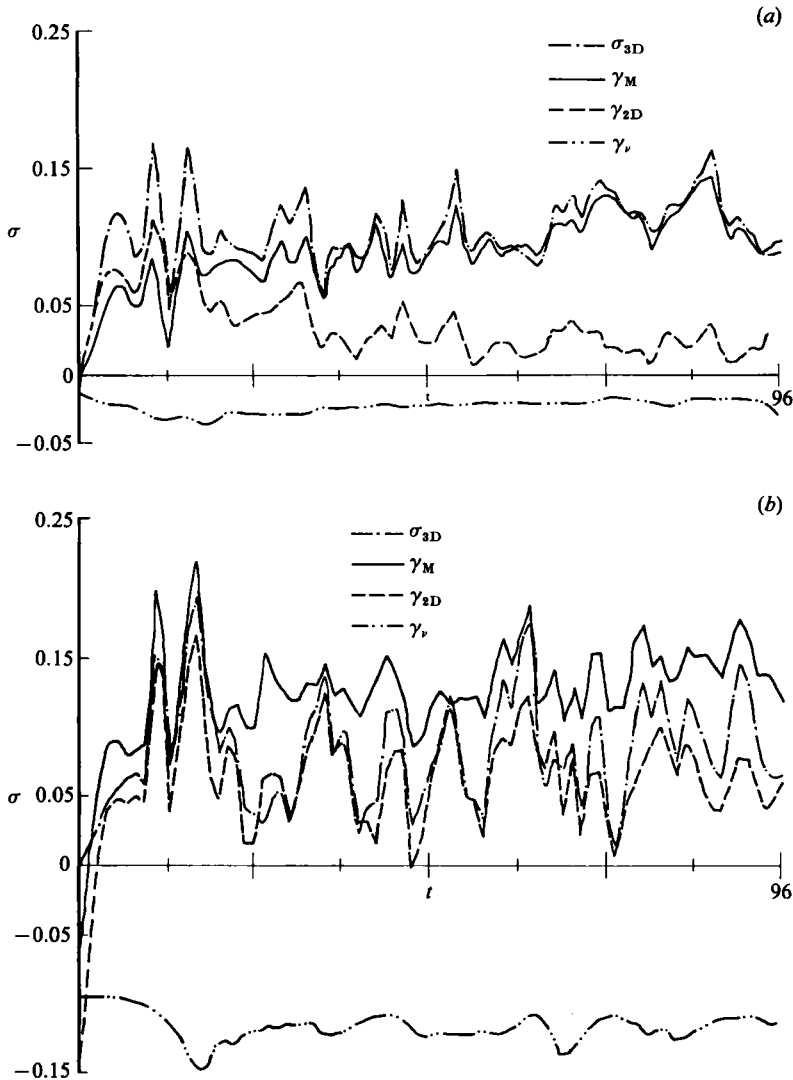


FIGURE 11. A plot of the components  $\gamma_M$ ,  $\gamma_{2D}$ ,  $\gamma_\nu$  (see (4.3)) of the three-dimensional growth rate  $\sigma_{3D}$  as functions of time for  $R = 400$ ,  $\alpha = 0.4$ ,  $A_{10} = 0.25$ ,  $A_{11} = 10^{-6}$ . (a)  $\beta = 4$ , (b) 6.

jitter in the plots is due to numerical inaccuracy in the evaluation of the nonlinear transfer terms, so only the trends in the data should be considered significant. It is suggested from the data in figure 11(a) that, for  $\beta < \beta_{crit}$ ,  $\gamma_\nu$  and  $\gamma_{2D} \ll \gamma_M$  (asymptotically as  $R$  becomes large) so that the three-dimensional mode derives its energy from the mean flow with the two-dimensional disturbance acting as a catalyst for this transfer.

On the other hand, the results plotted in figure 11(b) show that when  $\beta \approx \beta_{crit}$ ,  $\gamma_\nu$  is quite significant. The three-dimensional instability seems to be turned off at a large cross-stream wavenumber  $\beta$  by increased dissipation rather than by any significant qualitative change in nonlinear transfers from the mean and two-dimensional components.

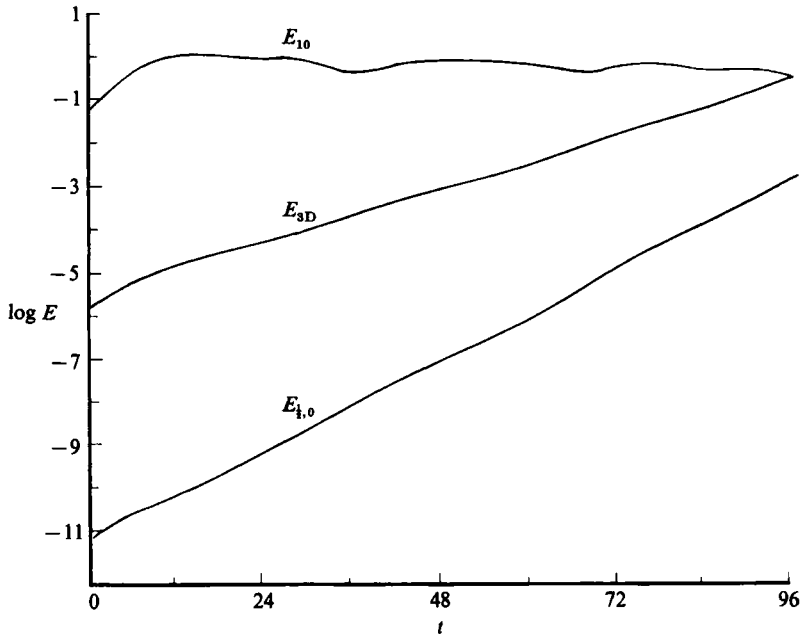


FIGURE 12. A plot of the evolution of the energies  $E_{10}$ ,  $E_{i,0}$ ,  $E_{3D}$  versus  $t$  for a run with  $R = 400$ ,  $\alpha = 0.4$ ,  $\beta = 0.2$ ,  $M = 8$ ,  $N = 4$ ,  $P = 32$ , and initial conditions  $A_{10} = 0.25$ ,  $A_{i,0} = 3 \times 10^{-6}$ ,  $A_{11} = 10^{-3}$ . The three-dimensional mode initially dominates the subharmonic mode.

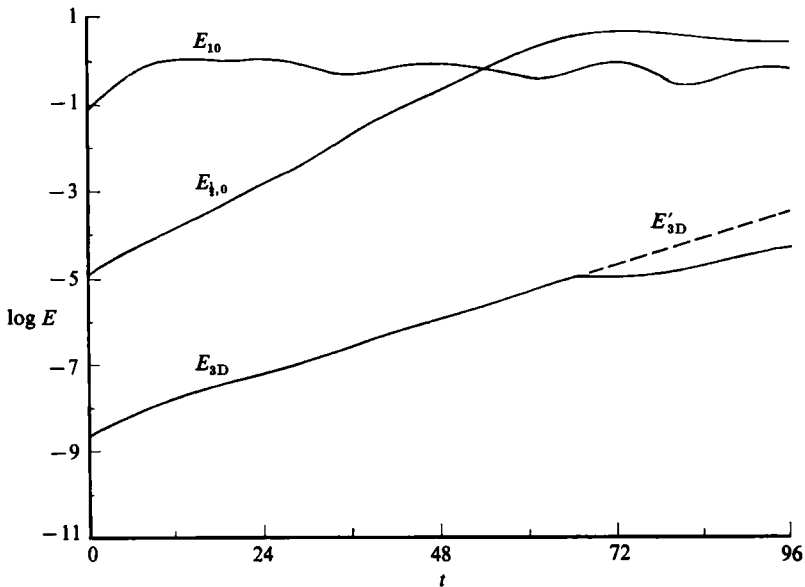


FIGURE 13. Same as figure 12, except that the initial conditions are  $A_{10} = 0.25$ ,  $A_{i,0} = 4 \times 10^{-3}$ ,  $A_{11} = 3.3 \times 10^{-5}$ . Here,  $E'_{3D} = 10^{-3} \times E_{3D}$  from figure 12. Note that the linear growth of the three-dimensional mode is stopped when the subharmonic reaches a nonlinear amplitude.

The nature of the competition between two-dimensional pairing and three-dimensional instability is illustrated by the results plotted in figures 12 and 13. In both figures, we have plotted the results of runs with  $R = 400$ ,  $\alpha = 0.4$  and  $\beta = 0.2$ . Figure 12 shows the evolution of the instabilities when the initial three-dimensional perturbation is much larger than the subharmonic mode. In this case, the pairing instability is nearly unaffected by the three-dimensional instability before finite amplitudes are reached. In figure 13, the initial conditions are chosen so that the subharmonic mode perturbation is much larger than that of the three-dimensional perturbation; it seems that the pairing process and roll-up inhibit the three-dimensional instability near  $t = 72$ , where  $\sigma_{3D}$  actually becomes negative. Note that the growth rate of  $E_{3D}$  is identical for the two cases (figures 12 and 13) until  $A_{1,0}$  reaches finite amplitude.

### 5. Instability: dependence on initial conditions

The flows that develop from the three-dimensional secondary instability do not appear to saturate in ordered states like those of the fundamental and subharmonic two-dimensional instabilities. However, the presence of additional pairing modes can significantly enhance the overall coherence of the flow. Experiments have shown that extremely low levels of forcing can generate changes in the flow of order 1 (e.g. Gutmark & Ho 1983). This has raised concerns that unintended forms of weak excitation due to natural resonances in an experimental apparatus, or pressure feedback effects, could be modifying the evolution of the flow field (Hussain 1983*b*). An important difference between our numerically simulated temporally growing flows and the spatially growing flows in laboratory experiments is that influences of downstream events on the earlier stages of evolution are possible in the latter but not the former.

In figure 14(*a*) we plot results that show the effect of the absence of a subharmonic pairing mode on the evolution of the modal energies. In the absence of the subharmonic, the fundamental quickly rolls up, a process that inhibits the growth of the low-amplitude three-dimensional disturbance. Once the fundamental reaches its saturated quasi-equilibrium state ( $t \approx 20$ ), the three-dimensional modes resume their rapid growth. By about  $t = 50$ , the three-dimensional modes dominate the flow field. The perspective plot given in figure 14(*b*) shows this domination even at later times. Further growth of the three-dimensional perturbation energy is inhibited by the collapse of the mixing layer due to the absence of the subharmonic. With the subharmonic present, the evolution of the three-dimensional modes is dramatically different. The results plotted in figure 14(*c*) are from a simulation identical with the previous one except for the inclusion of the subharmonic mode. The three-dimensional modal growth (at amplitudes in the linear range) is now slowed both by the fundamental roll-up ( $t \approx 5-10$ ) and by the subharmonic pairing ( $t \approx 20-35$ ). Thus, the flow is more coherent than in the absence of the subharmonic (compare figure 14*b* and *d*). After the subharmonic has reached its saturated state and no further pairing takes place, the three-dimensional growth rate increases substantially.

To determine whether the model used to initiate the three-dimensional instabilities in the simulations described thus far was realistic, we performed several simulations initialized with a broad range of three-dimensional modes. We used an uncorrelated, random-phase velocity field having a Gaussian-shaped energy spectrum. This field was convolved with a function so that the *relative* turbulence intensity levels were consistent with those of experimental mixing-layer data. However, the initial peak

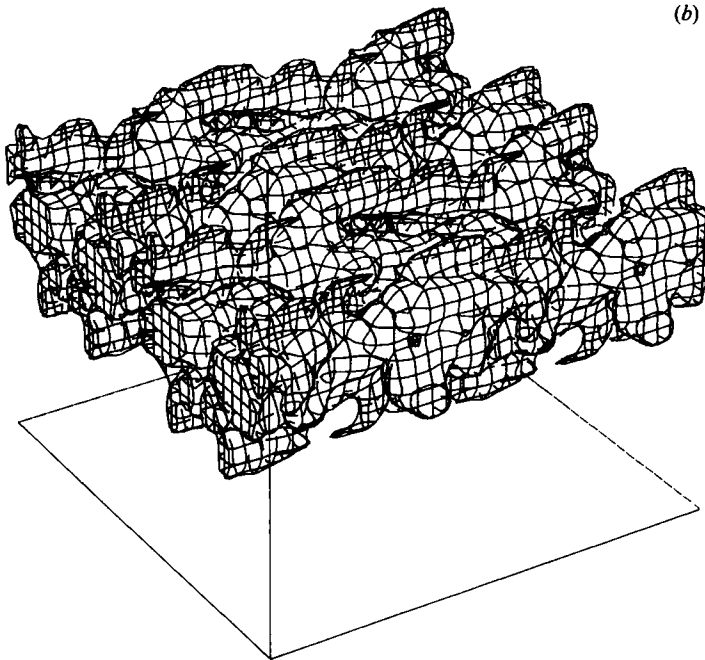
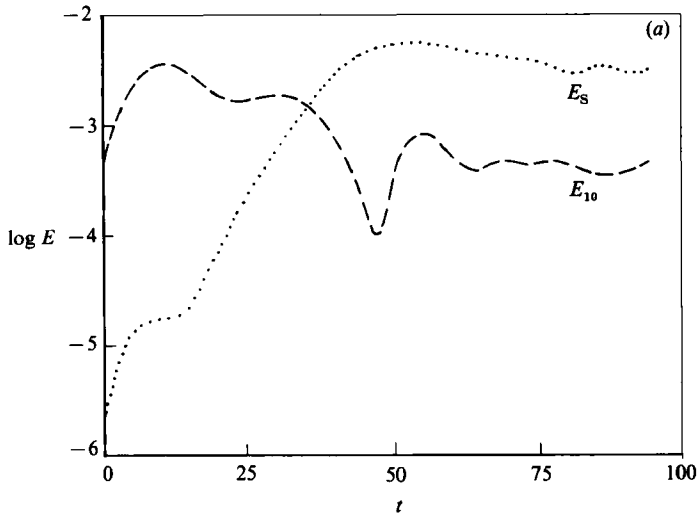


FIGURE 14(a, b). For caption see facing page.

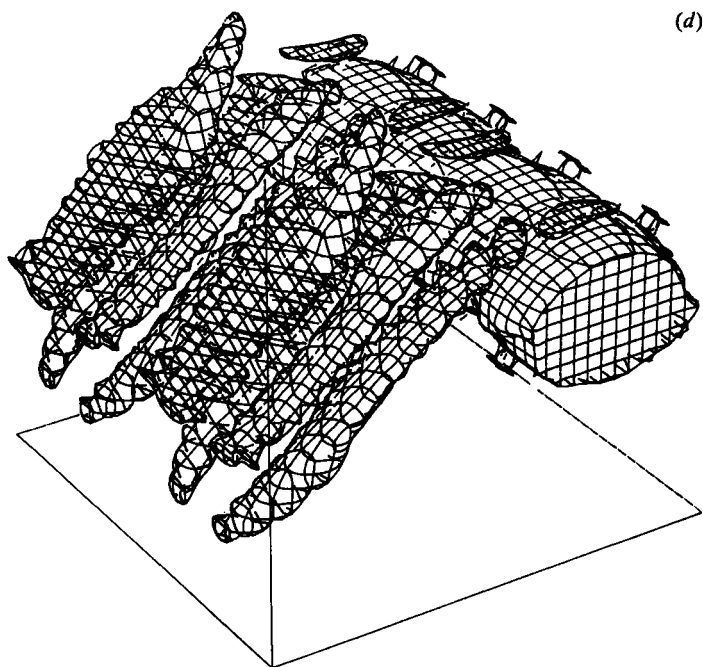
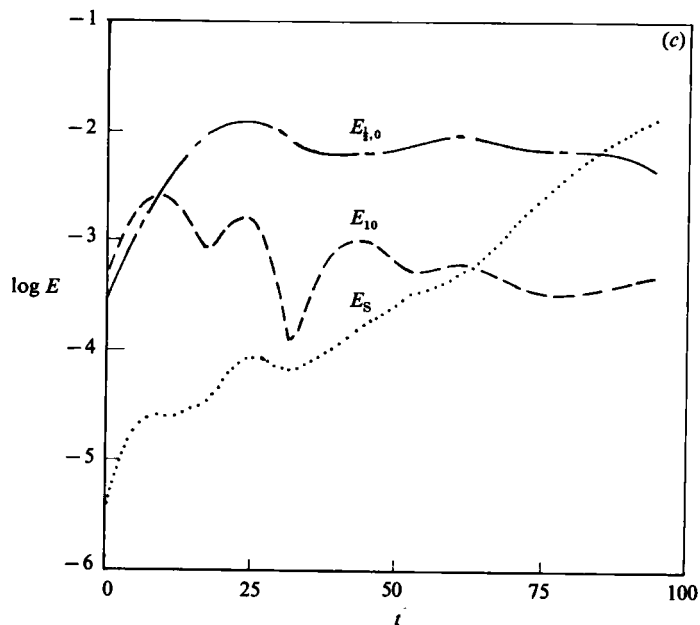


FIGURE 14. (a) A plot of the evolution of the modal energies as functions of time.  $E_S = E_{01} + E_{11} + E_{21}$ , i.e. the three lowest spanwise modes with the same  $x$ -wavelength as the fundamental.  $R = 100$ ,  $\alpha = 0.4446$ ,  $A_{10} = 0.22$ ,  $A_{i,0} = 0$  and  $A_{11} = 10^{-5}$ .  $M = N = P = 64$ . (b) A three-dimensional perspective plot of the vorticity field as in figure 10 at  $t = 96$ . (c) As (a) but  $A_{i,0} = 0.14$ . (d) As (b) but  $A_{i,0} = 0.14$ .

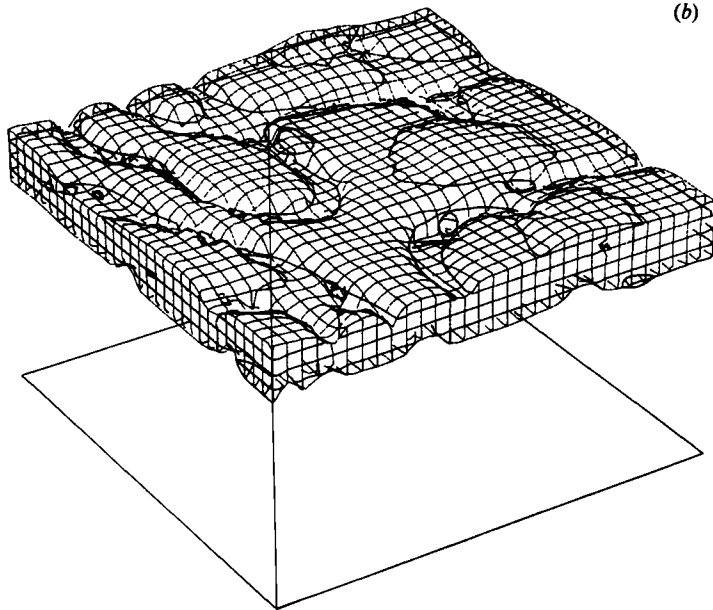
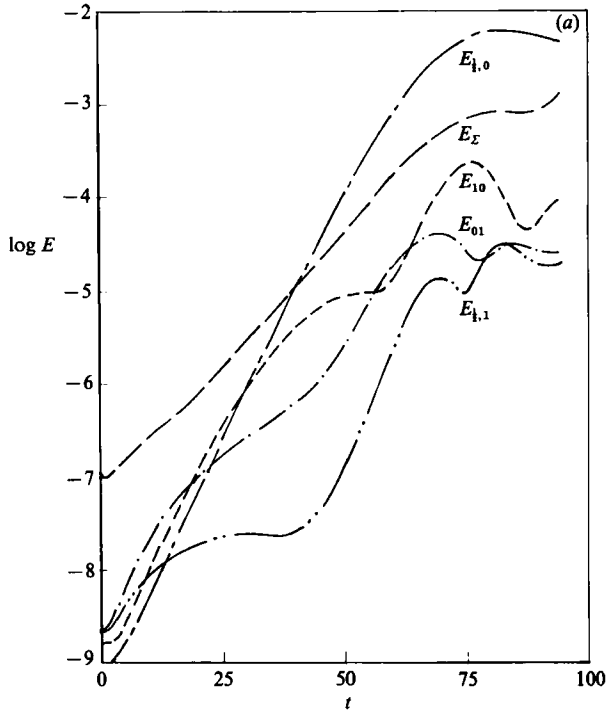


FIGURE 15(a, b). For caption see facing page.

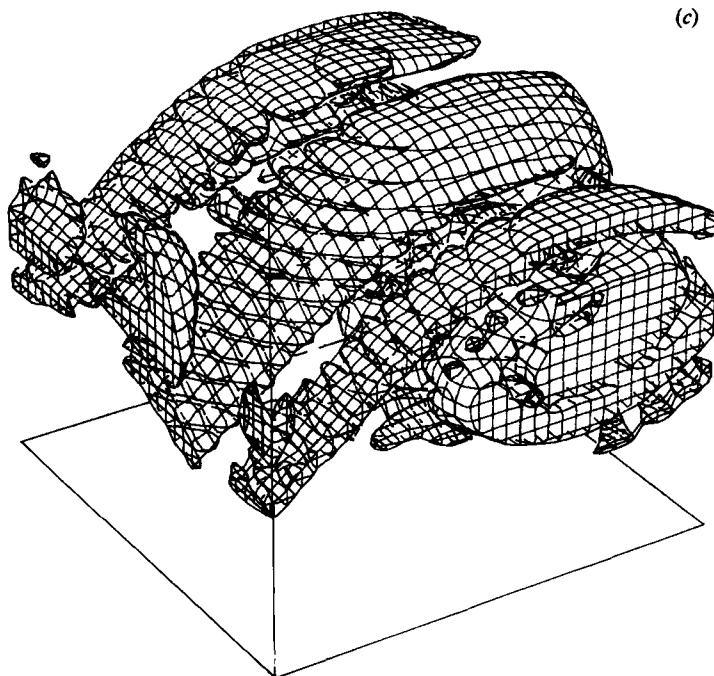


FIGURE 15. (a) A plot of the evolution of the modal energies as functions of time.  $E_{\Sigma}$  = energy in all modes with  $k_y \neq 0$ .  $R = 100$ . Random noise initial field with peak r.m.s. velocity  $\approx 0.01$ .  $M = N = P = 64$ . (b) A three-dimensional perspective plot of the vorticity field as in figure 10 at  $t = 48$ . (c) As (b) but at  $t = 96$ .

intensity level was about 3 orders of magnitude below the experimental values, so the initial disturbance growth was in the linear regime.

In figure 15(a) we plot the evolution of the flow field with broadband initial excitation. Neither fundamental nor subharmonic two-dimensional linear eigenfunction modes were explicitly included in the initial conditions, although there was energy in the corresponding wavenumbers defined by the random initialization process. Nonetheless,  $E_{10}$  and  $E_{\frac{1}{2},0}$  grow very rapidly initially, with  $\sigma_{10} = 0.13$  and  $\sigma_{\frac{1}{2},0} = 0.13$  at  $t = 10$  (compared with  $\sigma_{\frac{1}{2},0} = 0.19$  and  $\sigma_{10} = 0.14$  for linear inviscid eigenmodes).  $E_{\Sigma}$ , which is the energy in all velocity components not having  $k_y = 0$ , has a growth rate of  $\sigma_{3D} = 0.05$  at  $t = 10$ . It should be noted that these growth rates, while representative, do depend significantly on the particular flow-field initialization. In the early stages of the flow evolution, the flow is dominated by the three-dimensional modes, and the flow field takes on a less organized, more chaotic character (figure 15b). Eventually, the faster growing subharmonic comes to dominate the flow, changing it into a more ordered state with coherent, large-scale structures (compare figure 15b and c). The two most apparent components of these large-scale structures are the quasi-two-dimensional subharmonic and the streamwise, counter-rotating vortices. This clearly indicates the dominance of these two major modes of instability well into the range of nonlinear interaction.

Some aspects of the flow evolution are sensitive to Reynolds number. While we are under some severe constraints with regard to the maximum Reynolds number that can be accurately simulated due to computer resolution limitations, it is possible to examine some of the basic trends. Figures 16(a-c) correspond to figures 15(a-c),

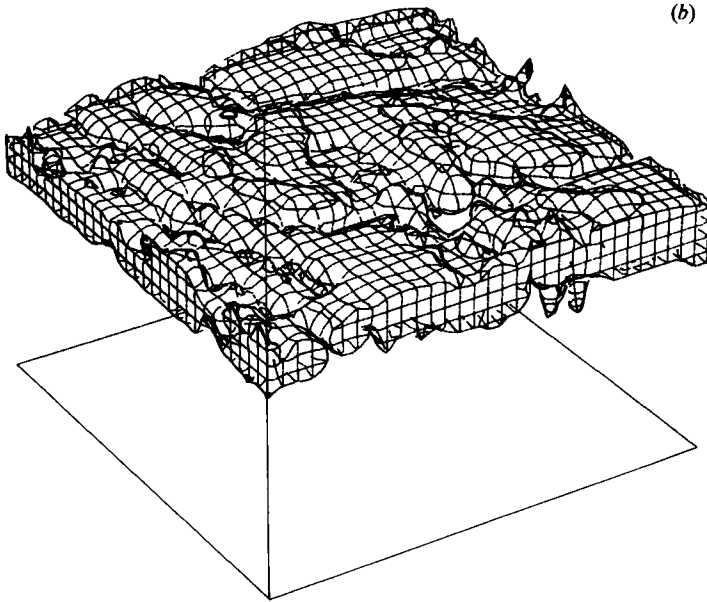
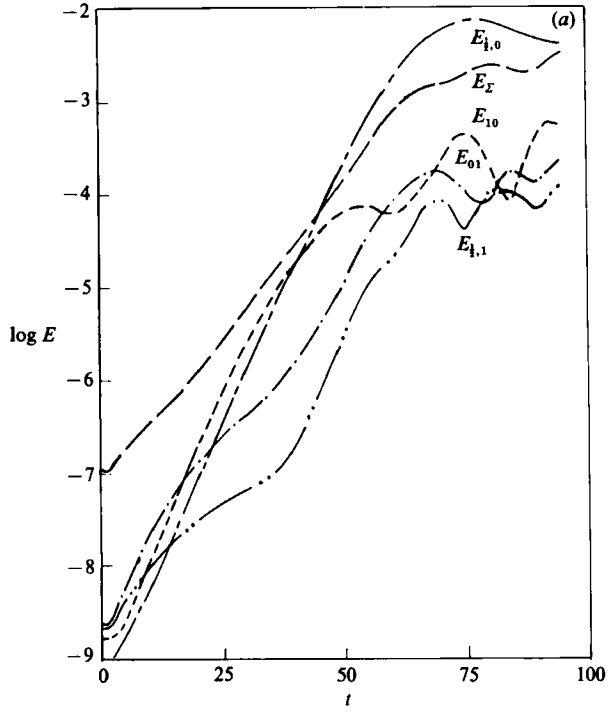


FIGURE 16(a,b). For caption see facing page.

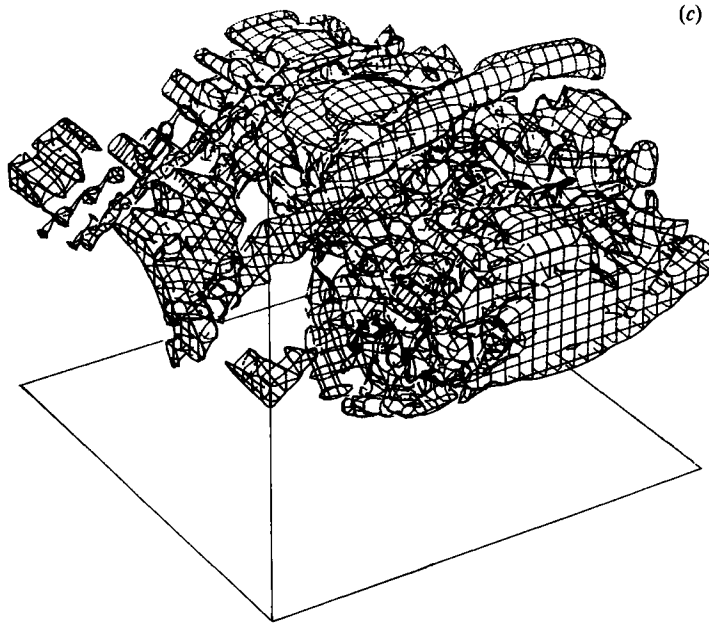


FIGURE 16. (a-c) As figure 15(a-c) but at  $R = 150$ .

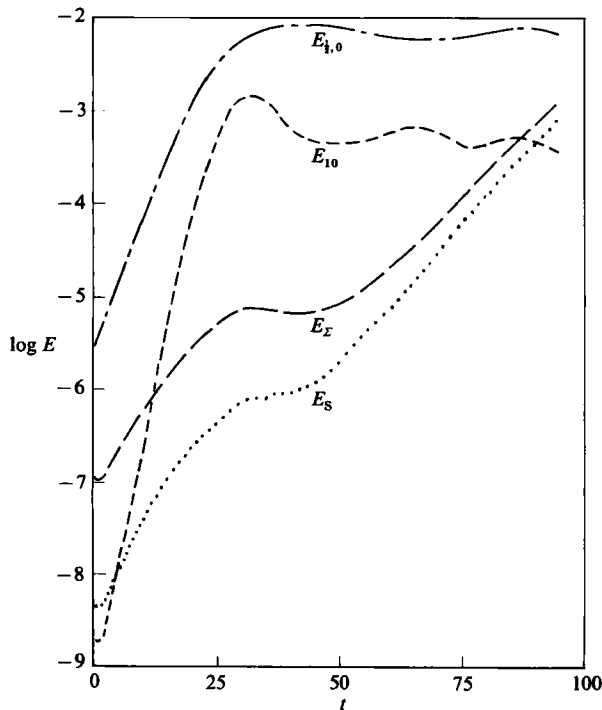


FIGURE 17. A plot of the evolution of the modal energies as functions of time.  $E_{\Sigma}$  = energy in all modes with  $k_y \neq 0$ .  $E_s = E_{01} + E_{11} + E_{21}$ .  $R = 100$ ,  $\alpha = 0.4446$ ,  $A_{10} = 0$ ,  $A_{i,0} = 0.0014$  and  $A_{11} = 10^{-5}$ .  $M = N = P = 64$ .

and are from a simulation with initial conditions identical with those in figure 15, but with an initial Reynolds number of 150 instead of 100. A comparison between figures 15(a) and 16(a) shows that, while the qualitative behaviour of most modes is similar, the growth rates of the three-dimensional modes are most significantly affected. This is consistent with the growth rate behaviour shown in figure 8. The increased amplitude of the three-dimensional modes as well as the presence of smaller scale instabilities at higher Reynolds numbers is apparent in figure 16(b, c). The Reynolds-number effect on the two-dimensional subharmonic mode  $E_{\frac{1}{2},0}$  is much less. It shows only a slight increase in growth rate, and still saturates at approximately the same amplitude, dominating the latter stages of the flow evolution.

The inhibition of the three-dimensional modal growth rate by the roll-up and pairing of the two-dimensional modes is a function of both the amplitude and the wavenumber of the three-dimensional modes. The presence of active pairing or roll-up by the coherent two-dimensional modes can actually stabilize low-amplitude three-dimensional modes. In figure 17, we plot the evolution of the modal energies as functions of time for a simulation with the same initial conditions as in figure 16 but with  $A_{\frac{1}{2},0} = 0.0014$ . As seen in this figure, when the subharmonic reaches nonlinear amplitudes ( $t \approx 25$ ), the three-dimensional growth is stopped completely. Since there was essentially no energy initially in the fundamental mode (i.e.  $A_{10} = 0$ ),  $E_{10}$  here represents approximately the harmonic energy component of the subharmonic mode (see footnote on page 213). While  $E_{10}$  is generally an order of magnitude or so less than  $E_{\frac{1}{2},0}$ , it becomes most significant just prior to saturation. During the three-dimensional stabilization shown in figure 17, the low- $\beta$  modes continue to grow while the high- $\beta$  modes decay. This is not unreasonable, since as the scale of the mixing layer grows owing to the two-dimensional pairing, the relative scale of the spanwise instability also changes. As shown in figure 8 for three-dimensional perturbations to two-dimensional saturated modes,  $\sigma_{3D}$  depends strongly on  $\beta$ . One mechanism that may have a significant influence on the suppression of the three-dimensional modal growth is the temporal variation of the strain field in the braids between the coherent, two-dimensional vortices. In the early stages of roll-up, a very high strain develops in the braids. This has a tendency to stretch the ribs, intensifying the streamwise vorticity. As the two-dimensional modes approach saturation, however, the strain rate decreases substantially, so that this vortex stretching mechanism is weakened.

## 6. The secondary instability in a turbulent flow

We have performed high-resolution ( $64 \times 64 \times 64$  mode) simulations of a fully turbulent mixing layer, and it is instructive to relate the evolution of these flows to the class of instabilities discussed so far. These simulations were performed on a computational domain sufficiently large to allow two complete pairings (periodicity length  $8\pi/\alpha$ ). The initialization procedure was similar to that discussed in §5, but the amplitudes of the initial fields were higher. Details of the numerics are given in Riley, Metcalfe & Orszag (1986).

The spanwise vorticity field after two complete pairings shows clear evidence of large-scale structures (see figure 18a, b). A comparison of the vorticity plots at two different spanwise locations indicates a strong spanwise coherence for this particular realization, although details of the structures are different. As previously noted, the secondary instabilities in the mixing-layer flow are characterized by streamwise, counter-rotating vortices that tend to form in the braids. Figure 19 is a contour plot of  $\omega_x$  in a plane at the middle of the mixing layer ( $z = 0$ ). The solid and dashed lines

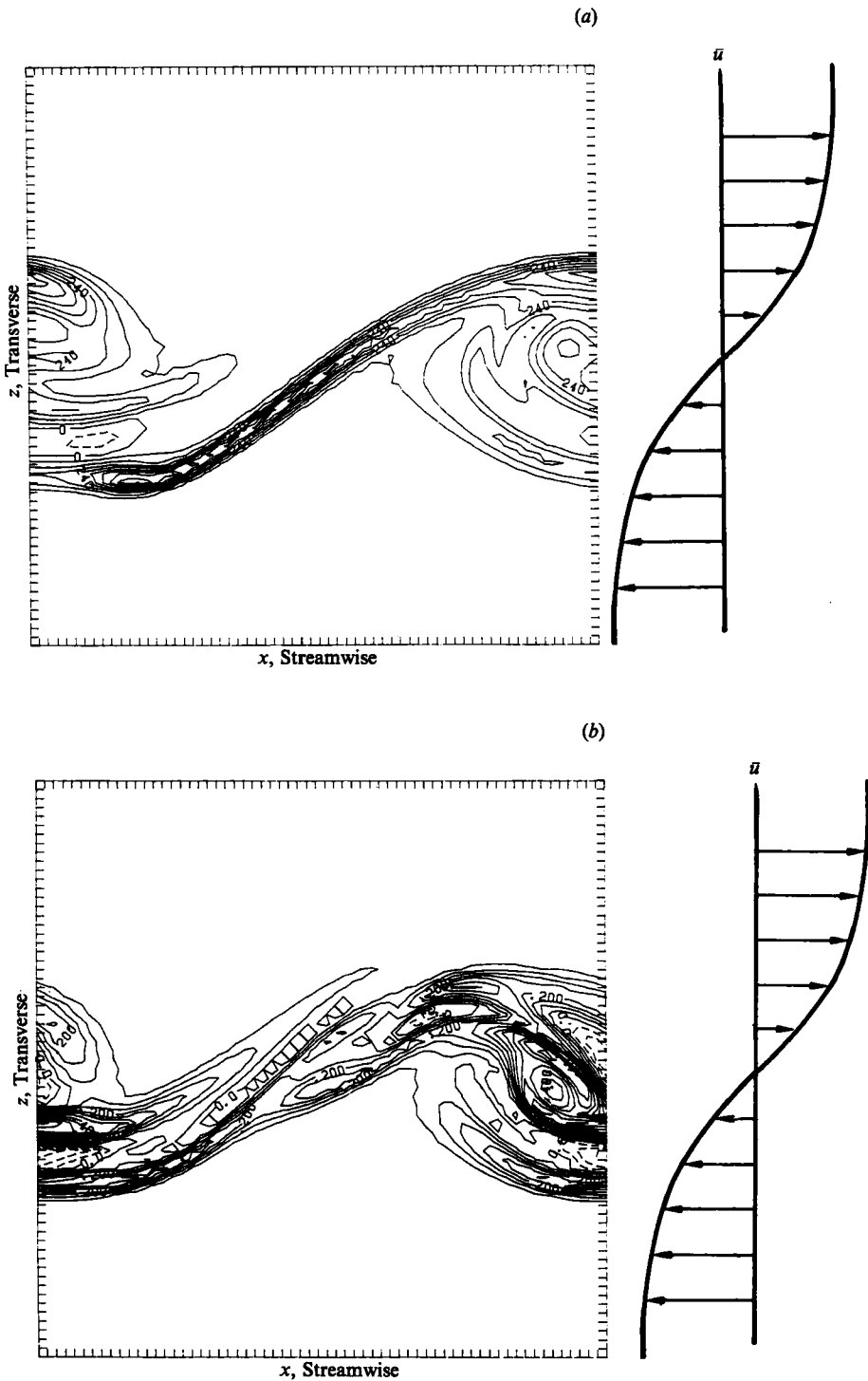


FIGURE 18. Spanwise vorticity at (a)  $y = 4\pi/\alpha$  and (b)  $6\pi/\alpha$ . The computational domain size  $B$  is  $8\pi/\alpha$ .  $R = 154$  and  $t = 72$ . Random noise initial field with peak r.m.s. velocity  $\approx 0.13$ . The initial Reynolds number is  $R = 28$ .  $M = N = P = 64$ .

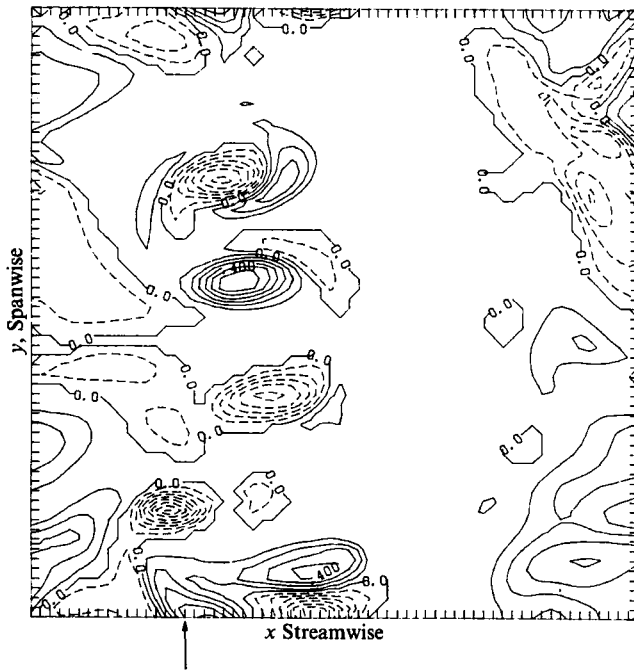


FIGURE 19. Streamwise vorticity at  $z \approx 0$  for the same run as in figure 18. Arrow indicates plane of figure 20.

indicate positive and negative vorticity, respectively. Figure 20 is a similar plot at a streamwise location  $2\pi/\alpha$  from the left boundary in figure 19. These two plots clearly indicate the presence of such vortices, although they are irregularly spaced.

One of the best laboratory visualizations of coherent, three-dimensional structures in a turbulent mixing layer was performed by Bernal & Roshko (cf. Bernal 1981; Jimenez, Cogolles & Bernal 1985; Bernal & Roshko 1986). Using laser fluorescein dye techniques, they were able to illuminate the flow at a fixed streamwise location. The most striking characteristic of these photographs is the appearance of mushroom-shaped features on the braids between the two-dimensional vortex cores (figure 21 *a*). Excellent experimental visualizations of these structures also appear in recent work by Lasheras, Cho & Maxworthy (1986). We have been able to simulate this technique by employing a numerical code developed to study a chemically reacting mixing layer (Riley *et al.* 1986) in which the advection–diffusion equations for a binary chemical reaction are solved along with the Navier–Stokes equations. Figure 21 (*b*) is a contour plot of the concentration of one of the chemical species on the same plane as in figure 20, and figure 21 (*c*) corresponds to the concentration of the other chemical species. A comparison of figures 20 and 21 (*b*) shows that the counter-rotating vortex pairs tend to pump fluid through the braid between their cores, increasing the reaction surface area and creating the mushroom-shaped structures in the flame front, which is defined by the region of overlap between figure 21 (*b, c*). Such features were also noted in the model proposed by Lin & Corcos (1984). Counter-rotating streamwise vortical structures are a key feature of tertiary instability studied by Nagata & Busse (1983).

The structure of the streamwise, counter-rotating vortex tubes is made clearer by isolating the streamwise vorticity component of the flow. Figure 22 is a three-dimensional perspective plot of surfaces at which  $|\omega_x|$  equals 50% of its peak value.

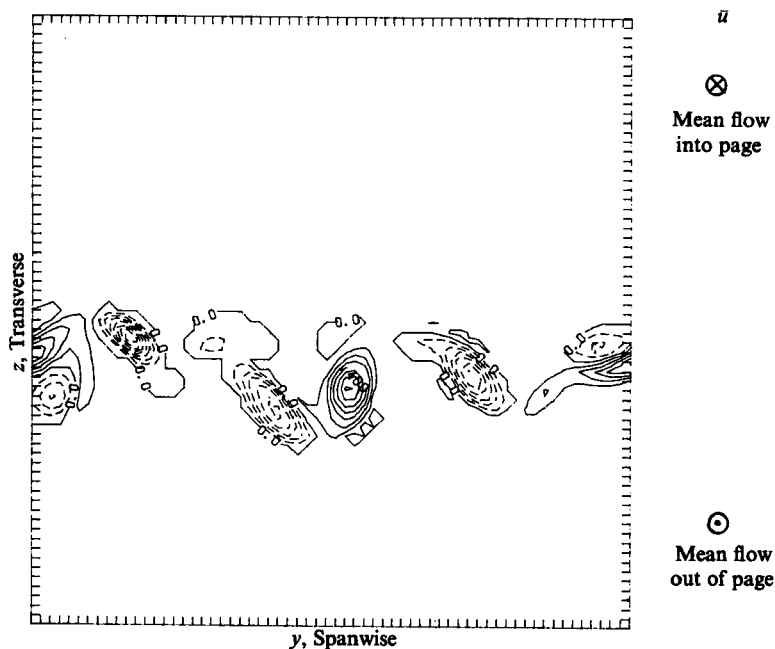


FIGURE 20. Streamwise vorticity at  $x = 2\pi/\alpha$  for the same run as in figure 18.

This figure was from the same realization and at the same time as figures 18, 19 and 21 (*b, c*). The large-scale, spanwise-coherent structures do not show up in this plot since they consist mainly of spanwise vorticity,  $\omega_y$ . Comparison with figures 18 (*a* and *b*) shows that the ribs do form on the braid between the large-scale two-dimensional vortex cores. This structure is consistent with the model proposed by Bernal (1981; Bernal & Roshko 1986) although the irregular spacing of the ribs suggests that the modification of this model proposed by Hussain (1983*a*) is more realistic. The effect of increased coherence of the two-dimensional pairing modes on the rib structure is shown in figure 23, which is from a simulation like the previous one but to which two-dimensional modes have been added in the initial conditions:  $A_{10} = 0.1$ ,  $A_{2,0} = 0.06$ ,  $A_{4,0} = 0.025$  (equation (3.1)). The resulting ribs are more coherent and more aligned in the streamwise direction. As was the case with the simulation in figure 16, the presence of the pairing mode tends to increase the coherence of the three-dimensional perturbation field.

The extreme sensitivity of the ribs to the initial or upstream flow conditions makes direct quantitative comparisons between the simulations and laboratory experiments difficult. In the simulations that we have performed so far, there have been significant variations in the amplitudes and spanwise spacing of the ribs. Likewise, in the experiments of Bernal (1981; Bernal & Roshko 1986), there was substantial scatter in the measurements of the rib spacing. In addition, he found that the spanwise position of the ribs appeared to be related to disturbances originating upstream in the settling chamber. Our stability analysis (figure 8) has shown that there is a broad range of spanwise wavenumbers that are unstable. Some representative values for the simulation shown in figures 18–22 are as follows: the peak spanwise vorticity normalized by the peak mean velocity gradient is about 2, while the peak streamwise vorticity is slightly higher, about 3. At the Reynolds numbers of our simulations, the

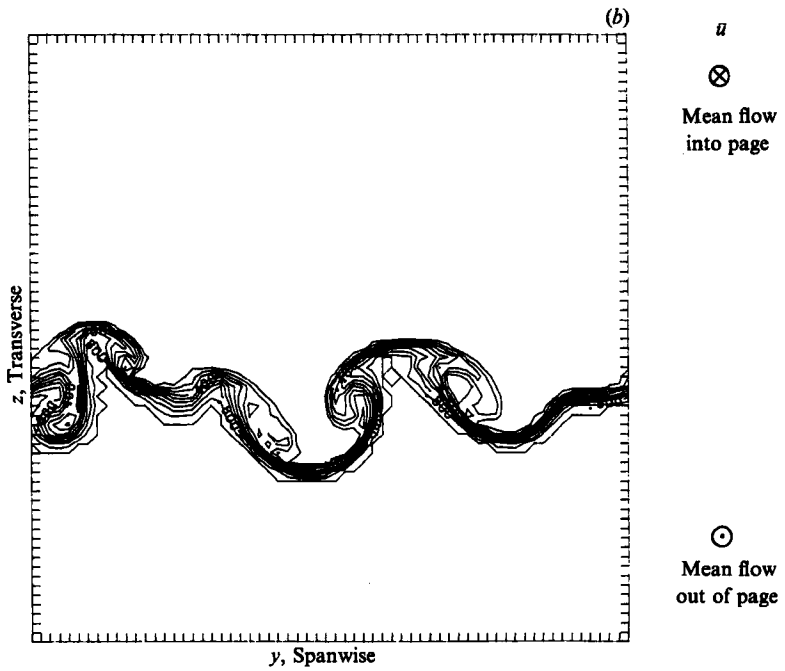
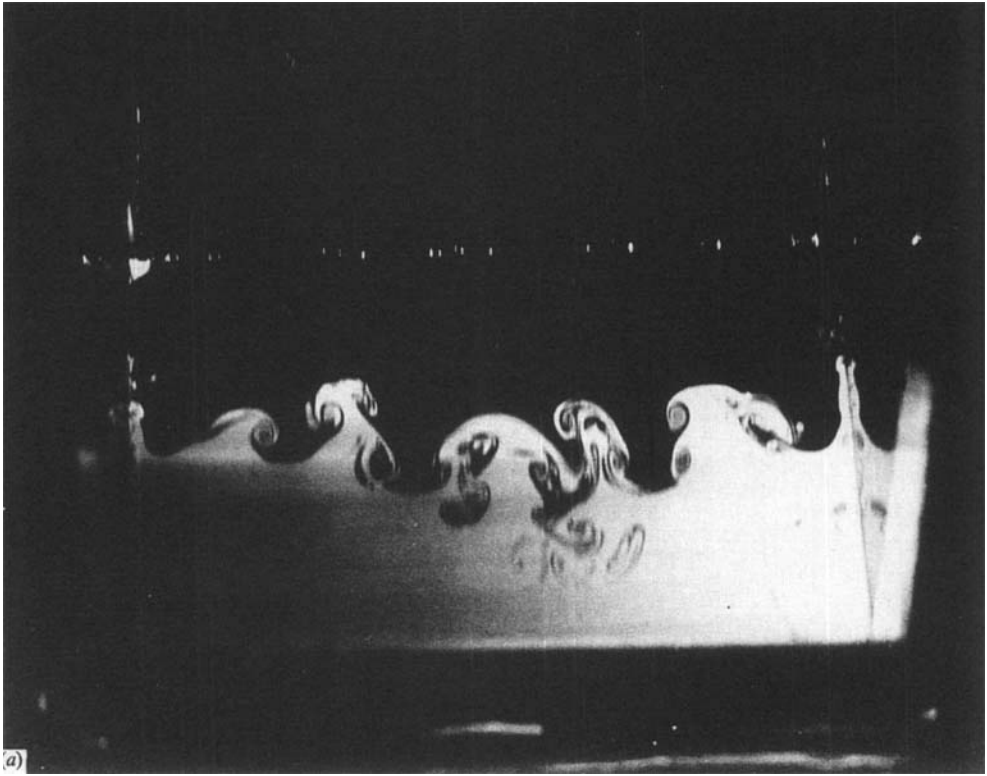


FIGURE 21 (*a, b*). For caption see facing page.

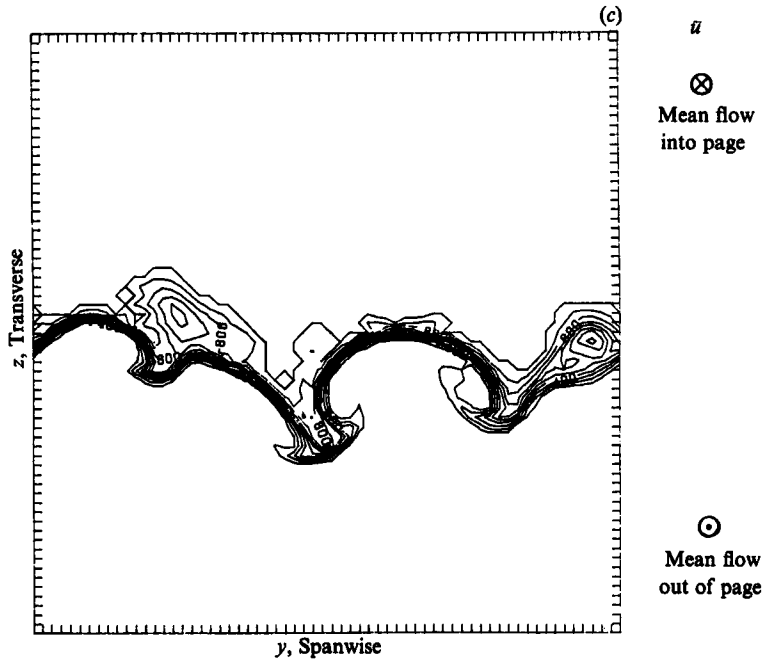


FIGURE 21. (a) Laser sheet/fluorescein dye visualization of the braid of a turbulent mixing layer in water (from Bernal 1981). (b) Contour plot of the species concentration field at the same time and location as in figure 20. (c) Contour plot of the second species concentration field at the same time and location as in (b).

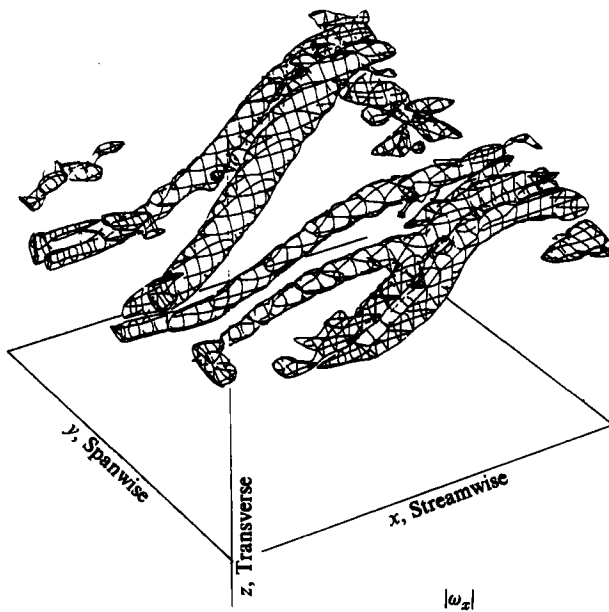


FIGURE 22. Three-dimensional perspective plot of surfaces at which  $|\omega_x|$  equals 50% of its peak value for the same run as in figure 18.

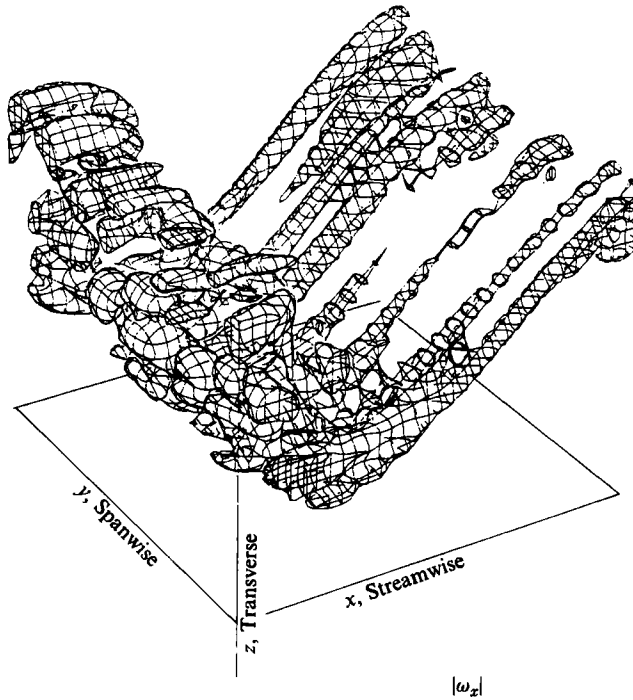


FIGURE 23. Plot of  $|\omega_x|$  as in figure 22 but for a simulation to which two-dimensional modes have been added in the initial conditions:  $A_{10} = 0.1$ ,  $A_{\frac{1}{2},0} = 0.06$  and  $A_{\frac{1}{4},0} = 0.025$  (equation (3.1)).

spanwise vorticity amplitudes are similar to filtered experimental data (Metcalf *et al.* 1987), while the streamwise vorticity amplitudes are somewhat higher than in other computed realizations. The rib spacing (estimated from figure 19) is about the same as the wavelength of the most unstable fundamental two-dimensional mode. This is in the range of values reported by Bernal (1981; Bernal & Roshko 1986). A more detailed analysis of these simulations, using experimental data to refine these comparisons, is now in progress.

## 7. Discussion

We have shown that small-scale three-dimensional instabilities exist in free shear flows at moderately low Reynolds numbers. It is now clear that these modes can be responsible for the initial development of three-dimensionality in these shear flows. At high amplitudes, these instabilities manifest themselves mainly as counter-rotating, streamwise vortices, or ribs, that form on the braids between the spanwise-coherent, two-dimensional pairing modes; they are responsible for the generation of the mushroom-shaped features seen in laboratory experimental visualizations (Bernal 1981; Bernal & Roshko 1986). While the instabilities share some features of a classical inflexional instability, including phase locking with the fundamental vortex, inflexional instabilities are preferentially two-dimensional, whereas the present instabilities are not. We have not yet been able to determine the precise relationship between the three-dimensional instabilities appearing in our simulations and the elliptical vortex-core instability studied by Pierrehumbert & Widnall (1982). An elegant quasi-analytical theory of this instability (Bayly 1986) shows that it is essentially a Floquet instability. Nonetheless, a careful analysis of our simulations

shows evidence of strong three-dimensionality within the spanwise vortex cores themselves. It is not yet clear whether the ribs are generated from an instability originating within the spanwise vortex cores, or whether other instability mechanisms come into play.

The roll-up and pairing of the two-dimensional modes has a stabilizing effect on the higher wavenumber spanwise modes and on the overall three-dimensional growth rate when the amplitude of the three-dimensional modes is small, while the absence of pairing (saturation) can enhance the three-dimensional growth rate. The suppression of the low-amplitude three-dimensional instabilities by pairing could explain the strong two-dimensionality of the flow near the splitter plate in many laboratory experiments. Once the three-dimensional modes reach a finite amplitude and/or the Reynolds number increases with downstream distance, the growth suppression effect is reduced, and the flow becomes more three-dimensional.

The results of these simulations suggest that, with respect to the growth of three-dimensional disturbances, there are several important flow states possible in an evolving mixing layer. First, there is pairing and roll-up of the two-dimensional modes, which is characterized by a suppression of low-amplitude three-dimensional modal growth at least at low Reynolds numbers. Secondly, in the presence of forcing, there is the saturated, two-dimensional, quasi-equilibrium, non-pairing state, which is highly unstable to three-dimensional perturbations. Our simulations show that, even from highly chaotic, three-dimensional flow states, more rapidly growing, large-scale, two-dimensional modes can eventually emerge and reorganize the flow in a manner consistent with that suggested by Lesieur, Staquet & Le Roy (1987).

It seems that the mechanics of transition in the free shear flows studied here may, in a sense, be rather more complicated than in the case of wall-bounded shear flows. In the latter case, linear instabilities are often viscously driven and, therefore, weak, so they cannot be directly responsible for the rapid distortions characteristic of transition. On the other hand, free shear flows are subject to a variety of inviscid instabilities, so there may be many paths to turbulence. We have shown that the choice of paths in any individual flow may depend on the results of competition between fundamental, subharmonic and three-dimensional instabilities, all of which are convectively driven and, therefore, strong with comparable growth rates. Thus, the evolution of free shear flows in transitional regimes depends significantly on the past history of the flow, including the relative amplitudes of all competing modes, the mechanism of their generation and the external environment in which the flow is embedded.

This work was supported by the Office of Naval Research under Contracts N00014-82-C-0600 and N00014-82-C-0451, the National Science Foundation under Grants ATM-84-1410, MSM-85-14128 and MSM-83-19804 and the Air Force Office of Scientific Research under Contract F49620-85-C-0026. The computations reported here were performed at the computing facilities of the National Aeronautics and Space Administration Ames and Lewis Research Centers and the National Center for Atmospheric Research, Boulder, Colorado, which is supported by the National Science Foundation. The authors have benefited from discussions with a number of colleagues including A. K. M. F. Hussain, C.-M. Ho, M. Morkovan and Gilles Corcos and appreciate the capable assistance of Donald Lovell with certain aspects of the computer programming. We would also like to thank Dr Luis P. Bernal and Professor Anatol Roshko for permission to use their flow visualization photograph (figure 21*a*). R. W. M. performed the work while at Flow Research Company, Kent, WA 98032.

## REFERENCES

- BAYLY, B. J. 1986 Three-dimensional instability of elliptic flow. *Phys. Rev. Lett.* **57**, 2160–2164.
- BERNAL, L. P. 1981 The coherent structure of turbulent mixing layers. I. Similarity of the primary vortex structure. II. Secondary streamwise vortex structure. Ph.D. thesis, California Institute of Technology, Pasadena.
- BERNAL, L. P., BREIDENTHAL, R. E., BROWN, G. L., KONRAD, J. H. & ROSHKO, A. 1979 On the development of three dimensional small scales in turbulent mixing layers. In *Proc. 2nd Intl Symp. on Turbulent Shear Flows*. Imperial College, London.
- BERNAL, L. P. & ROSHKO, A. 1986 Streamwise vortex structure in plane mixing layers. *J. Fluid Mech.* **170**, 499–525.
- BRACHET, M. E., MEIRON, D. I., ORSZAG, S. A., NICKEL, B. G., MORF, R. H. & FRISCH, U. 1983 Small-scale structure of the Taylor–Green vortex. *J. Fluid Mech.* **130**, 411–452.
- BREIDENTHAL, R. 1981 Structure in turbulent mixing layers and wakes using a chemical reaction. *J. Fluid Mech.* **109**, 1–24.
- BROWAND, F. K. & TROUTT, T. 1980 A note on spanwise structure in the two-dimensional mixing layer. *J. Fluid Mech.* **97**, 771–781.
- BROWAND, F. K. & TROUTT, T. R. 1985 The turbulent mixing layer: geometry of large vortices. *J. Fluid Mech.* **158**, 489–509.
- BROWN, G. L. & ROSHKO, A. 1974 On density effects and large structures in turbulent mixing layers. *J. Fluid Mech.* **64**, 775–816.
- BUSSE, F. H. & CLEVER, R. M. 1979 Instabilities of convection rolls in a fluid of moderate Prandtl number. *J. Fluid Mech.* **91**, 319–335.
- CAIN, A. B., FERZIGER, J. H. & REYNOLDS, W. C. 1984 Discrete orthogonal function for non-uniform grids using the fast Fourier transform. *J. Comp. Phys.* **56**, 272–286.
- COLLINS, D. A. 1982 A numerical study of the stability of a stratified mixing layer. Ph.D. Thesis, Department of Mathematics, McGill University, Montreal.
- CORCOS, G. M. & LIN, S. J. 1984 The mixing layer: deterministic models of a turbulent flow. Part 2. The origin of the three-dimensional motion. *J. Fluid Mech.* **139**, 67–95.
- CORCOS, G. M. & SHERMAN, F. S. 1984 The mixing layer: deterministic models of a turbulent flow. Part 1. Introduction and the two-dimensional flow. *J. Fluid Mech.* **139**, 29–65.
- DRAZIN, P. G. & REID, W. H. 1981 *Hydrodynamic Stability*. Cambridge University Press.
- FREYMUTH, P. 1966 On transition in a separated laminar boundary layer. *J. Fluid Mech.* **25**, 683–704.
- GUTMARK, E. & HO, C.-M. 1983 Preferred modes and the spreading rates of jets. *Phys. Fluids* **26**, 2932–2938.
- HO, C.-M. & HUANG, L.-S. 1982 Subharmonics and vortex merging in mixing layers. *J. Fluid Mech.* **119**, 443–473.
- HO, C.-M. & HUERRE, P. 1984 Perturbed free shear layers. *Ann. Rev. Fluid Mech.* **16**, 365–424.
- HO, C.-M. & NOSSEIR, N. S. 1981 Dynamics of an impinging jet. Part 1. The feedback phenomenon. *J. Fluid Mech.* **105**, 119–142.
- HUSSAIN, A. K. M. F. 1983*a* In *Turbulence and Chaotic Phenomena in Fluids* (ed. T. Tatsumi), p. 453. North-Holland.
- HUSSAIN, A. K. M. F. 1983*b* Coherent structures – reality and myth. *Phys. Fluids* **26**, 2816–2850.
- HUSSAIN, A. K. M. F. & ZAMAN, K. B. M. Q. 1978 The free shear layer tone phenomenon and probe interference. *J. Fluid Mech.* **87**, 349–383.
- JIMENEZ, J., COGOLLOS, M. & BERNAL, L. P. 1985 A perspective view of the plane mixing layer. *J. Fluid Mech.* **152**, 125–143.
- KELLY, R. E. 1967 On the stability of an inviscid shear layer which is periodic in space and time. *J. Fluid Mech.* **27**, 657–689.
- KLAASSEN, G. P. & PELTIER, W. R. 1985 The onset of turbulence in finite-amplitude Kelvin–Helmholtz billows. *J. Fluid Mech.* **155**, 1–35.
- LASHERAS, J. C., CHO, J. S. & MAXWORTHY, T. 1986 On the origin and evolution of streamwise vortical structures in a plane, free shear layer. *J. Fluid Mech.* **172**, 231–258.

- LESIEUR, M., STAQUET, C. & LE ROY, P. 1987 The mixing layer and its coherence examined from the point of view of two-dimensional turbulence. *J. Fluid Mech.* (submitted).
- LIN, S. J. & CORCOS, G. M. 1984 The mixing layer: deterministic models of a turbulent flow. Part 3. The effect of plane strain on the dynamics of streamwise vortices. *J. Fluid Mech.* **141**, 139–178.
- LOWERY, P. S., REYNOLDS, W. C. & MANSOUR, N. N. 1987 Passive scalar entrainment and mixing in a forced, spatially-developing mixing layer. *AIAA Paper* 87-0132.
- METCALFE, R. W., HUSSAIN, A. K. M. F., MENON, S. & HAYAKAWA, M. 1987 Coherent structures in a turbulent mixing layer: A comparison between direct numerical simulations and experiments. In *Proc. 5th Symp. Turbulent Shear Flows* (ed. F. Durst, B. E. Launder, F. W. Schmidt & J. H. Whitelaw), pp. 110–123. Springer.
- MICHALKE, A. 1964 On the inviscid instability of the hyperbolic tangent velocity profile. *J. Fluid Mech.* **19**, 543–556.
- MIKSAD, R. W. 1972 Experiments on the nonlinear stages of free layer transition. *J. Fluid Mech.* **56**, 695–719.
- NAGATA, M. & BUSSE, F. H. 1983 Three-dimensional tertiary motions in a plane shear layer. *J. Fluid Mech.* **135**, 1–26.
- ORSZAG, S. A., ISRAELI, M. & DEVILLE, M. O. 1986 Boundary conditions for incompressible flow problems. *J. Sci. Computing* **1**, 75–111.
- ORSZAG, S. A. & PAO, Y. 1974 Numerical computation of turbulent shear flows. *Adv. Geophys.* **18A**, 225–236.
- ORSZAG, S. A. & PATERA, A. T. 1980 Subcritical transition to turbulence in plane channel flows. *Phys. Rev. Lett.* **45**, 989.
- ORSZAG, S. A. & PATERA, A. T. 1983 Secondary instability of wall-bounded shear flows. *J. Fluid Mech.* **128**, 347–385.
- OSTER, D. & WYGNANSKI, I. 1982 The forced mixing layer between parallel streams. *J. Fluid Mech.* **123**, 91–130.
- PATNAIK, P. C., SHERMAN, F. S. & CORCOS, G. M. 1976 A numerical simulation of Kelvin–Helmholtz waves of finite amplitude. *J. Fluid Mech.* **73**, 215–240.
- PIERREHUMBERT, R. T. & WIDNALL, S. E. 1982 The two- and three-dimensional instabilities of a spatially periodic shear layer. *J. Fluid Mech.* **114**, 59–82.
- RILEY, J. J. & METCALFE, R. W. 1980 Direct numerical simulation of a perturbed, turbulent mixing layer. *AIAA Paper* 80-0274.
- RILEY, J. J., METCALFE, R. W. & ORSZAG, S. A. 1986 Direct numerical simulations of chemically reacting turbulent mixing layers. *Phys. Fluids* **29**, 406–422.
- STUART, J. T. 1967 On finite amplitude oscillations in laminar mixing layers. *J. Fluid Mech.* **29**, 417–440.
- WINANT, C. D. & BROWAND, F. K. 1974 Vortex pairing: the mechanism of turbulent mixing-layer growth at moderate Reynolds number. *J. Fluid Mech.* **63**, 237–255.
- WYGNANSKI, I., OSTER, D., FIEDLER, H. & DZIOMBA, B. 1979 On the perseverance of a quasi-two-dimensional eddy-structure in a turbulent mixing layer. *J. Fluid Mech.* **93**, 325–335.